UNIVERSITÀ DEGLI STUDI DI PADOVA

Dipartimento di Fisica e Astronomia "Galileo Galilei"

Photonics and Optoelectronics Group, LMU Munich

Corso di Laurea in Fisica

Tesi di Laurea

Energy Transfer Processes in Lead Halide Perovskite Quantum Dots

Relatore

Prof. Giovanni Mattei

Correlatore

Dr. Quinten Akkerman

Laureando

Alessandro Zamboni

Anno Accademico 2023/2024

Abstract

Due to their unique optoelectronic properties colloidal lead halide perovskite quantum dots (LHP QDs) have received much attention in the recent years. With a near-unity photoluminescence (PL) quantum yield and highly tuneable PL of small spectral width, this group of materials is of interest for research and applications such as light-emitting devices and photovoltaics. The solution processability of colloidal QDs makes them compabtible with various manufacturing techniques like spin-/spray-coating and injekt printing. Together with the scalability of colloidal synthesis, this might offer a pathway for industrial use in future applications. However, colloidal quantum dots are surrounded by a shell of ligands, stabilizing them in solution and preventing aggregation. These ligands can act as energy barriers between QDs, hindering efficient charge and energy transfer, therefore impairing the performance of QD-based devices (e.g., charge carrier extraction in solar cells). Within the scope of this work, different size $CsPbBr_3$ QDs are synthesized and energy transfer processes are investigated using time-resolved photoluminescence spectroscopy. In particular, the influence of various ligands of varying carbon chain length on these processes is studied.

Grazie alle loro peculiari proprietà optoelettroniche, i quantum dots colloidali di perovskite di alogenuro di piombo (LHP QDs) hanno ricevuto molta attenzione negli ultimi anni. Con una resa quantica di fotoluminescenza (PL) prossima all'unità e una PL altamente sintonizzabile di piccola ampiezza spettrale, questo gruppo di materiali è di interesse per la ricerca e per applicazioni quali dispositivi a emissione di luce e il fotovoltaico. La processabilità in soluzione dei QDs colloidali li rende compatibili con varie tecniche di produzione come lo spin-/spray-coating e l'injekt printing. Insieme alla scalabilità della sintesi dei colloidi, questo potrebbe offrire un percorso per l'uso industriale in applicazioni future. Inoltre, i quantum dots colloidali sono circondati da un guscio di ligandi che li stabilizza in soluzione e ne impedisce l'aggregazione. Questi ligandi possono agire come barriere energetiche tra i QDs, ostacolando il trasferimento efficiente di carica ed energia e quindi compromettendo le prestazioni dei dispositivi basati sui QDs (ad esempio, l'estrazione dei portatori di carica nelle celle solari). Nell'ambito di questo lavoro, sono stati sintetizzati QDs di $CsPbBr_3$ di diverse dimensioni e ne sono stati studiati i processi di trasferimento di energia utilizzando la spettroscopia di fotoluminescenza risolta nel tempo. In particolare, viene studiata l'influenza di vari ligandi di diversa lunghezza della catena di carbonio su questi processi.

Acknowledgements

This thesis work has been done during my exchange period at the Ludwig Maximilian University (LMU) of Munich. The experimental work has been carried out entirely at Nanoinstitute of the LMU, Chair for Photonics and Optoelectronics of Prof. Jochen Feldmann, whom I thank very much for giving me the opportunity to work with one of his research groups in high-quality laboratories and in a scientifically stimulating environment.

I am really grateful to both my internal and external supervisor. To Prof. Giovanni Mattei for giving me precious insights and advices on the work and for the administrative support. To Dr. Quinten Akkerman for introducing me to physics research, for showing me what it means to be in a scientific group, and for making me think about what I was doing; although the communication was not always easy, I think this thesis period really made me mature as a physicist.

Mariam Kurashvili and Anja Barfüßer were the two people that really guided me through the project, helping me with the synthesis, showing me how to use the spectrometers, explaining me how to analyze the data and how to interpret the results, always being available when I needed it. Thank you for your time! Thanks also to David Ederle who helped me with the synthesis.

Contents

Chapter 1

Introduction

Semiconductors and semiconductor devices have become, since the second half of the last century, essential in many aspects of our society, from the use in electronics due to the development of transistors to the conversion of solar energy to electricity in solar cells. The recent development of nanotechnology, is bringing us a new generation of semiconductor structures that will consolidate the strategic importance semiconductors have in our society, for instance in enabling a smoother shift to renewable energy resources and in development of quantum technologies. In this context quantum dots are emerging as one of the most promising platforms, presenting potential applications as single-electron transistors, in display technology, solar cells, LEDs, qubits for quantum information processing and as single photon sources .

The interesting optical properties of semiconductor quantum dots (or semiconductor nanocrystals quantum confined in 3 dimensions), such as band gap tunability, come from their zero dimensional structure, which confines the charge carriers enhancing their light emission. In particular for these reasons, in the last years quantum dots of lead halide perovskites have attracted the attention of diverse scientists due to a serie of properties such as optical versatility, high photoluminescence quantum yield, facile synthesis and high tolerance to structural defects and surface states [1].

Starting from these assumptions, this thesis will focus on lead halide perovskite nanocrystals of $CsPbBr_3$. The theoretical aspects of semiconductor quantum dots will be first introduced, highlighting the properties relevant for the experimental work, as well as an introduction to the main energy transfer processes between quantum dots. The chemical synthesis of the colloidal quantum dots will be shown, as well as the main experimental methods used to investigate the optical properties, such as steady-state and time-resolved photoluminescence spectroscopy. The last chapter contains the experimental work. The main aim of the thesis is to study how different sized quantum dots interact between each other when mixed together, so how smaller and more energetic quantum dots (QDs) yield energy to larger and less energetic ones, and how these transfers change when the distance between quantum dots in a sample is increased or decreased. In particular, this will be done using two different ligands of different length, both when the sample is deposited on a film and when it is dispersed in solution. In conclusion, the experimental results are discussed and analyzed, several parameters are derived from the experimental data and the presence of Förster-type resonance energy transfers is proven.

Chapter 2

Theory

2.1 Electronic and optical properties of semiconductors

In order to understand the optical properties of the perovskite QDs, we first need to take a look at the electronic properties of a semiconductor, starting from the crystal structure of solids. The condition of periodicity of a physical quantity A in a crystal is given by $A(\vec{r}) = A(\vec{r} + \vec{R})$, where $\vec{R} = \sum_i n_i \vec{a}_i$, with n_i integers gives an infinite array of discrete points named Bravais lattice, with $\vec{a}_i$, $i = 1, 2, 3$ being the primitive vectors. The Fourier transform of such lattice gives its dual vector space in the $\vec{k}$-space, known as reciprocal lattice. The Brillouin zone (BZ) is the Wigner-Seitz cell of the reciprocal lattice, and all the physical processes inside the crystal can be represented here for symmetry reasons.

When sufficient energy is given to the system, the lattice ions oscillate if some oscillations modes are permitted. A phonon is a quasiparticle that represents such excited state of the modes of vibration. Such oscillation modes can be either acoustic, if the oscillation of the cores is in phase, or optical, if the unit cell consists of more than one atom and the oscillation is out of phase [2] [3].

2.1.1 Electronic band structure derivation and statistics of charge carriers

The Hamiltonian operator of a crystalline solid consisting of M ion cores and N valence electrons is given by

$$\hat{H} = -\sum_{j=1}^{M} \frac{\hbar^2}{2m_j} \nabla^2_{\vec{R}_j} - \sum_{i=1}^{N} \frac{\hbar^2}{2m_0} \nabla^2_{\vec{r}_i} + \frac{1}{4\pi\epsilon_0} \left(\sum_{j>j'} \frac{e^2 Z_j Z_{j'}}{|\vec{R}_j - \vec{R}_{j'}|} + \sum_{i>i'} \frac{e^2}{|\vec{r}_i - \vec{r}_{i'}|} + \sum_{i,j} \frac{e^2 Z_j}{|\vec{r}_i - \vec{R}_j|} \right) \quad (2.1)$$

where $\vec{R}_j$ and $\vec{r}_j$ denote the core and electron positions respectively, Z_j the atomic number of the core, m_j and m_0 the core and electron mass, ϵ_0 the vacuum permittivity. In order to describe the physical properties of a crystal, one should find the eigenvalues of the Hamiltonian solving the corresponding Schrödinger equation $\hat{H}\psi(\vec{r_i}, \vec{R_j}) = E\psi(\vec{r_i}, \vec{R_j})$. This is however practically impossible (there are roughly 10^{23} particles per cm^3) and some approximations are needed. The Born-Oppenheimer (BO) approximation is based on the fact that the nuclei are much heavier than the electrons, and therefore electrons follow instantaneously the movement of the cores, but not vice versa. In the BO approximation the wavefunction can be expressed as a product of an electronic and a nuclear part, $\psi = \psi_{\text{electron}} \psi_{\text{core}}$, which enables a separation of the Hamiltonian in electronic and nuclear term, neglecting cross-terms between electrons and nuclei.

Another approximation that comes into play in many electrons systems is the independent electron approximation: if the electron-electron interaction term is sufficiently small, the Coulomb interaction terms can be treated as an effective potential term $V(\vec{r})$ which neglects the electron-electron interaction, allowing us to decompose the electronic part of the Hamiltonian into a set of N decoupled

Hamiltonians (one for each electron). The Schrödinger equation for a single electron is then given by

$$\left(-\frac{\hbar^2}{2m_0}\nabla^2_{\vec{r}} + V(\vec{r})\right)\psi_{\text{electron}} = E\psi_{\text{electron}} \tag{2.2}$$

For lattice ions occupying an equilibrium position, the surrounding potential can be treated as parabolic, leading to an harmonic approximation, valid for small dislocations. This potential is periodic because of the periodicity of the crystal lattice, so $V(\vec{r}+\vec{R}) = V(\vec{r})$. Bloch's theorem states that the solutions of equation 2.2 in a periodic potential can be expressed as plane waves modulated by periodic functions, written as $\psi_{\text{electron}}(\vec{r}) = e^{i\vec{k}\vec{r}}u(\vec{r})$ (Bloch waves), where $u(\vec{r})$ is a periodic wavefunction with the same periodicity as the crystal, so $u(\vec{r}) = u(\vec{r}+\vec{R})$. The resulting energy solutions of 2.2 as a function of $\vec{k}$ form the electronic band structure. Because of the periodic potential, our approximation differs from a free electron model, and its parabolic dispersion is slightly altered, with energy gaps appearing at the borders of the BZ, as can be seen in figure 2.1, where it is not possible to have electrons. A reduced zone scheme representation of the dispersion relation in the 1st BZ is also possible.

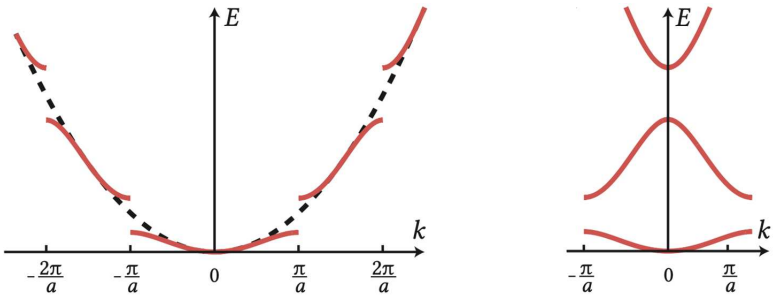

Figure 2.1: Left: energy gaps appearing at the borders of the BZs. Right: reduced zone schema. Figure adapted from [4].

For tightly bounded electrons, the electronic band structure can be derived considering the single atomic orbitals (AOs), and the valence electrons in the outer shells involved in bonding. When atoms are bond they form a molecule and the single AOs are combined (hybridization). The shape of the new molecular orbitals (MOs) can be determined using the linear combination of atomic orbitals (LCAO) approach. The linear combination of the atomic orbitals is given by the linear combination of the wave functions, (which for two AOs can be either constructive, $\psi = \psi_A + \psi_B$, or destructive, $\psi = \psi_A - \psi_B$), forming MO bonding orbital and MO antibonding orbital. The bonding orbital has a lower energy and is the first to be occupied by the electrons. More complex molecules lead to more complex MOs, composed by the linear combination of many AOs and involving also different bonds. In this case certain orbitals will hybridize forming bonding and anti bonding orbitals, while others might remain unchanged depending on the overlap of the different shaped orbitals.

Maxima and minima can be often represented approximately by a parabolic dispersion. Not all the energetic levels of the electronic structure are occupied by electrons though. At 0K, all the energetic levels below the Fermi energy E_F are occupied. The first two closest bands below and above to the Fermi energy are called conduction and valence band (CB and VB, with the second one lying energetically below E_F). If it happens that the Fermi energy lies within the CB and VB without touching them, the solid is a nonmetal, while if the two bands overlap for some $\vec{k}$ points or the Fermi energy lies within a partially filled energy band, the solid is a metal. In nonmetals therefore, the valence band is the highest energetic level where electrons are present at zero temperature, while the conduction band is the lowest energetic level where electrons are absent.

While for metals the conduction is always guaranteed, in nonmetals it is possible just in some cases, depending on the spacing between the two bands. The difference in energy between the valence band maximum and the conduction band minimum is referred to as bandgap energy E_g; if $0 \lesssim E_g \lesssim 4\,\text{eV}$

the material is a semiconductor (SC), while if E_g is larger the material is an insulator (note that exist so called wide-bandgap semiconductors that have even energetically larger bandgaps). Examples of E_g for some materials are reported in table 2.1. If the VB maximum and the CB minimum are at the same point of the $\vec{k}$-space, the bandgap is direct, otherwise indirect (from here the difference between direct and indirect SCs).

In a semiconductor, when an electron is excited some reasons from the VB to the CB, the hole left behind in the VB can be treated as a positively charged quasiparticle, quasi-free to move in the VB. The approximated parabolic curvature of CB minima and VB maxima is given by the following equation:

$$\frac{1}{m^*_{e/h}} = \frac{1}{\hbar^2}\left|\frac{\partial^2 E_{CB/VB}(\vec{k})}{\partial \vec{k}^2}\right| \tag{2.3}$$

where it has been introduced the effective mass m^* of the electron and hole, so the mass these seem to have as a result of the interaction with other particles in the crystal lattice. Electrons and holes in a periodic potential can be described similarly as free electrons or holes considering the effective mass. The valence band states derive from atomic p-orbitals; depending on the total angular momentum quantum number, heavy-hole (HH, $j = \frac{3}{2}$ and $m_j = \pm\frac{3}{2}$) and light-hole (LH, $j = \frac{3}{2}$ and $m_j = \pm\frac{1}{2}$) bands are formed, and similarly spin-orbit coupling effects lead to a split-off band lower in energy with $j = \frac{1}{2}$ (split-off holes, especially for SCs consisting of heavy atoms). Examples of effective masses for some materials are listed in table 2.1.

Material	E_g (eV)	Electron effective mass	(Heavy) hole effective mass
Si (300K)	≈ 1.12	≈ 1.09	≈ 1.15
Ge (300K)	≈ 0.67	≈ 0.55	≈ 0.37
GaAs (300K)	≈ 1.42	≈ 0.067	≈ 0.45
InP (300K)	≈ 1.34	≈ 0.079	≈ 0.45
$CsPbBr_3$	≈ 2.29	≈ 0.34	≈ 0.37

Table 2.1: Energy bandgaps and effective mass of charge carriers for some SCs, given in units of the free electron mass m_0. Here is reported for hole the heavy hole mass only. The values for $CsPbBr_3$ refer to the cubic phase. If the temperature is not reported, it was not indicated in the references [5] [6].

To describe the occupation statistics of such bands, we consider the density of states (DOS), so the electronic states available per unit energy range at a given energy level. The number of states in the system whose energy lies within E and $E + dE$ is given by $N(E)dE$, with $D(E) = \frac{N(E)}{V}$ being the density of states, defined as

$$D(E) = \frac{1}{V}\sum_{i=1}^{N_l} \delta\left(E - E(\vec{k})\right) \tag{2.4}$$

where V is the volume of the crystal, δ the Dirac delta function, N_l the number of energy levels. For a certain temperature T, the number of electrons occupying a certain energy level E_i follows the Fermi-Dirac distribution

$$\bar{n}_i = \frac{1}{e^{\frac{E_i - \mu}{k_B T}} + 1} \tag{2.5}$$

where $\mu(T)$ is the chemical potential, with $\mu(0) = E_F$. Therefore, for non-null temperatures the average number of electrons in the CB is $\neq 0$, and increasing the temperature more electrons are likely to jump from the VB to the CB and contributing to the conductivity of the semiconductor.

2.1.2 Carrier generation, recombination and light emission

To have electric conductivity, the electrons need to be able to move around in the material, so they need to be excited in order to reach the CB. We have seen in the previous section how, for non-zero

temperatures, the CB is partially filled with electrons. An electron can get excited to the CB also through the absorption of a photon (2.2 **a**). If the photon absorbed has an energy larger than the bandgap, the electron is excited to the CB and freely move through the empty orbitals.

The transition probability per unit of time from the initial state $|i\rangle$ to the final state $|f\rangle$ due to the interaction with a photon (described as a weak perturbation) is given, to first-order approximation, by Fermi's golden rule [2]

$$\Gamma_{i\to f} = \frac{2\pi}{\hbar} \left|\langle i| H' |f\rangle\right|^2 D(E_f \pm \hbar\omega) \tag{2.6}$$

where H' is the perturbing Hamiltonian, given by $H' = -e\vec{r}\vec{E}$ in the electric dipole approximation, and $D(E_f)$ is the density of states at the energy E_f of the final states.

Energy and momentum have to be conserved during the transition. In particular, the electron will have energy and momentum given by the intersection between the dispersion relation of the photon $E = \hbar\omega(\vec{k}) = \hbar c \left|\vec{k}\right|$ and the energy band level, as can be seen in figure 2.2 (being the dispersion relation much steeper in reality than in the picture, purely optical transitions can be approximated as vertical in the energy band diagram).

In an indirect bandgap semiconductor, for an interband transition to be possible, in addiction to the absorbed photon needs to be absorbed or emitted a phonon (2.2 **e**). Since a third particle is needed to jump across the bandgap, it is significantly less probable to excite electrons in an indirect bandgap semiconductor compared to a direct one.

If the electron is excited high into the CB can lower its energy dissipating it as heat (phonons), reaching the CB edge. This process is called relaxation. The electrons recombine then with the hole (recombination, 2.2 **b**) emitting a photon with the same energy as the band gap. This process is called radiative recombination, and it is the main form of photoluminescence (PL) in semiconductors (this process is slower for indirect bandgap semiconductor, where an additional phonon is required like in 2.2 **f**). The rate at which electrons recombine with their holes is called radiative recombination decay rate, k_r, and it is strongly material dependent. The radiative carrier life time is given by $\tau_r = \frac{1}{k_r}$.

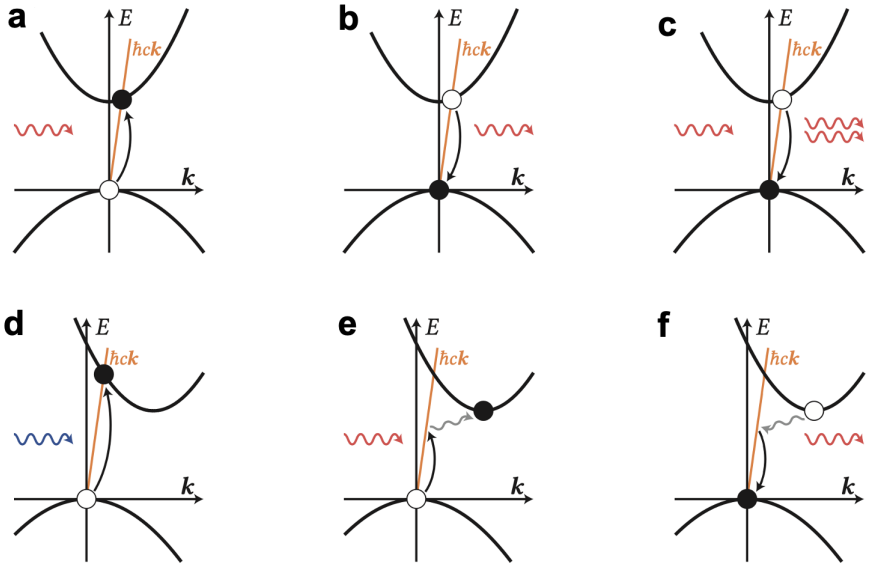

Figure 2.2: Different types of optical transitions: **a** the electron jumps to the CB after the absorption of a photon, leaving a hole behind; **b** radiative recombination with the emission of a photon; **c** stimulated emission; **d** absorption for an indirect bandgap requires a more energetic photon; **e** sometimes a phonon is required to reach the CB; **f** the phonon is required also when the carriers recombine. Image taken from [4].

It also is possible that an electron and hole recombine without the emission of a photon. Defects in the crystal lattice (for instance atoms missing or misplaced, chemical impurities etc.) tend to form

so-called trap states in the band gap of the semiconductor. These trap states result in less hybridized MOs and new occupable energetic levels within the two bands, where electrons and holes tend to move usually through the emission of a phonon. If the electron and hole recombine in this way, this results in a non radiative recombination (non radiative recombination processes due to defects can impair devices that require radiavite combination, such as LEDs and lasers, or that need to extract electrons, like solar cells). A particular type of trap states, so called surface trap states, less detrimental in bulk materials but more significant in semiconductors with smaller size like nanocrystals, where a relevant percentage of the atoms lies on the surface, are usually caused by dangling bonds and vacancies between the surface atoms. The non radiative recombination decay rate $k_{nr} = \frac{1}{\tau_{nr}}$ comprehend all these processes of recombination that do not result in the emission of light, and the quantum efficiency or photoluminescence quantum yield (PLQY) of a material is the ratio

$$\text{PLQY} = \frac{k_r}{k_r + k_{nr}} = \frac{1/\tau_r}{1/\tau_r + 1/\tau_{nr}} \leq 1 \tag{2.7}$$

that therefore depends on the quality and presence of defects in the material. The carrier lifetime is obtained from both type of events

$$\frac{1}{\tau} = \frac{1}{\tau_r} + \frac{1}{\tau_{nr}} \tag{2.8}$$

Other recombination processes are also possible, like the Auger recombination, where the energy of an electron-hole pair is transferred to a third charge carrier which is excited to a higher energy level without moving to another energy band, losing then its excess energy non radiatively through thermal vibrations.

2.1.3 Quantum confinement of excitons

An electron being excited in the CB and its respective hole in the VB are particles with an opposite electric charge and therefore can bound together due to Coulomb interaction. If this happens, the electric neutral bound state formed is called an exciton, and it is a quasiparticle able to travel through the lattice without any net transfer of charge. Depending on the strength of the Coulomb interaction between the particles, one can distinguish between more free to move throughout the crystal Wannier–Mott excitons and more tightly bound Frenkel excitons (with the first ones mainly observed in semiconductors, while the seconds in insulators) [2]. Excitons occupy a certain "space" and have a certain radius, with Wannier-Mott excitons having a larger radius due to their small binding energy.

For a Wannier-Mott exciton energy and radius can be derived, without solving the Schrödinger equation in analogy with the hydrogen atoms radius, considering furthermore the electrostatic screening due to the other atoms in the lattice with a relative permittivity ϵ, and replacing the electron mass with the reduced mass $\mu = \left(\frac{1}{m_e^*} + \frac{1}{m_h^*}\right)^{-1}$. The latter contains the mass corrections deriving from the electrostatic interaction of other particles in the lattice. Applying with such conditions the Bohr Model, we obtain the following equation for the energy levels of the excitons [4]

$$E_{exciton} = E_g + \frac{\hbar^2 K^2}{2\mu} - \frac{R_X}{n^2} \tag{2.9}$$

where n is the principal quantum number, $R_X = \frac{\mu}{m_0 \epsilon^2} R_H$ is the exciton Rydberg energy, R_H the Rydberg energy of the hydrogen atom and $\vec{K} = \vec{k_e} + \vec{k_h}$ the excitonic wave vector. The excitonic radius is instead given by

$$r_n = \frac{m_0}{\mu} \epsilon n^2 a_H = n^2 \, a_X \tag{2.10}$$

with $a_X = \frac{m_0 \epsilon}{\mu} a_H$ being the exciton Bohr radius and a_H the Bohr radius. Excitons can only form and remain stable when the exciton binding energy is larger than the thermal energy at a given temperature. In an absorption spectrum, a series of excitonic absorption lines are expected just

below the bandgap. The resulting expression in equation 2.10 is heavily material dependent with, for instance, CdSe, InAs and PbTe having an exciton radius of 5, 29 and 104 nm respectively (n=1). Free excitons are tipically seen in direct band gap semiconductors (but also indirect such as pure silicon or germanium, even though electrons and holes have different $\vec{k}$ vectors).

In semiconductors significantly larger than its exciton Bohr radius, an exciton can move freely through the crystal lattice; but what happens if the sizes of the semiconductor and the exciton are about the same? The exciton movement is no longer free, but spatially confined in one or more dimensions, and if the size of the semiconductor becomes smaller than the exciton Bohr radius the exciton energy increases (similarly to a particle in-a-box [7]). Due to this quantum confinement effect, the bandgap of the semiconductor and so its energy increases when decreasing the SC's size, and this can lead to a change in the optical properties of the shrinked semiconductor compared to its bulk counterpart. Depending on in how many dimensions this quantum confinement happens, different nanostructures (low-dimensional structures) can be created. Quantum-confined structures in 1-D are called quantum wells, in 2-D quantum wires and in 3-D quantum dots. Depending on the number of dimensions confined, these structures have a different electron density of states (DOS), that is $\sim E^{\frac{1}{2}}$ for the bulk, step-like $\sim E$ (constant) for quantum wells, $\sim E^{-\frac{1}{2}}$ for quantum wires, and discrete with only certain discrete energies allowed for quantum dots.

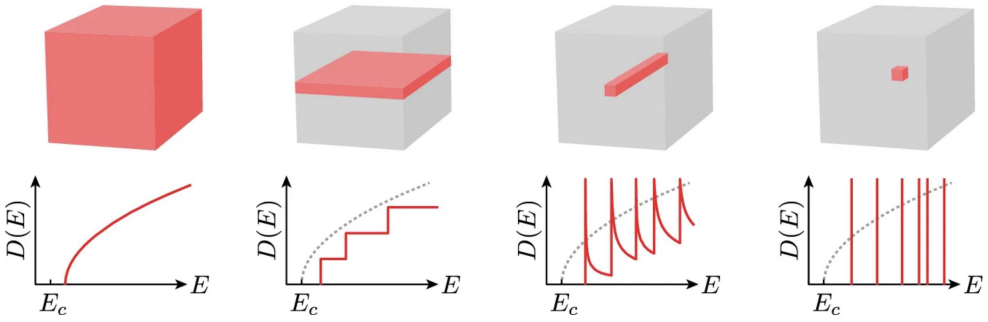

Figure 2.3: Low-dimensional structures and their respective DOS; from left to right: bulk SC, quantum well, quantum wire and quantum dot. Image taken from [8].

2.2 Quantum dots

In this section we focus on the physics of the quantum dots, as well as their chemical structure and the use of the ligands as coating. Quantum dots typically contain 10^4-10^6 atoms [2], and can be made by various techniques, such as molecular beam epitaxy (MBE), metal-organic chemical vapor deposition (MOCVD), or colloidal synthesis, used to obtain QDs spherical in shape. The emission energy of a QD, depending on its radius, is given by Brus equation [9]:

$$E_{QD} = E_g + E_{exciton} + \frac{\hbar^2 \pi^2}{2\mu r_{QD}^2} \tag{2.11}$$

with r_{QD} being the radius of the QD and μ the reduced mass.

QDs obtained by colloidal synthesis show a certain size distribution, and since different size QDs emit at different energies, this brings to an additional inhomogeneous broadened emission and absorption spectra. Other than this, it is present a fundamental homogeneous broadening, which consists a FWHM at 0 K of $\Delta E = \gamma$ for a single emitter. This Lorentzian broadening comes from the finite lifetime of the excited state due to the Heisenberg uncertainty principle. For temperatures $\neq 0$ the line shape is additionally broadened by other mechanisms, such as scattering processes between charge carriers and phonons.

Smaller QDs require high energy for the electrons to enter in the excited states, as seen in equation 2.11, and therefore they will emit light with smaller wavelength (see for example figure 2.5). Larger QDs instead have a smaller bandgap and emit light with larger wavelength. The most common QDs are often binary compositions of II-VI elements such as CdE, PbE, ZnE, with E=S,Se,Te, or ternary compositions like $CuInS_2$ or $CsPbX_3$, where X=Cl,Br,I, but it is also possible to combine more than one semiconductor domain in a single core, creating so called hetero nanocrystals (for example, core–shell semiconducting nanocrystals are made of a semiconducting core and a shell of a distinct semiconducting material, with the shell providing a passivation of the surface trap states increasing the quantum yield [10]). In table 2.2 are reported the core composition, QD size and exciton Bohr radius for some common QDs. The shape of a "spherical" QD is not perfectly spherical:

Core composition	Diameter (nm)	Exciton Bohr radius (nm)
ZnSe	$\approx$ 4.3-6.0	$\approx$ 8
CdSe	$\approx$ 1.0 up to 25	$\approx$ 5
CdS	$\approx$ 1.0-6.0	$\approx$ 2.7
$CsPbBr_3$	$\approx$ 4.0-10	$\approx$ 3.5

Table 2.2: Core composition, size range and exciton Bohr radius of some common QDs [11] [4] [12] [2]. A 20 nm $CsPbBr_3$ NC for instance will not exhibit any quantum confinement effect as its size is larger than the exciton radius.

QDs need simultaneously to grow large low energy planes, that makes them assume the structure of truncated spheres, with so-called facets on the surface, as can be seen in figure 2.4.

Since size and shape affect heavily the optical properties of a NC, it is important to control these properties during the synthesis of the quantum dots. In order to do so, ligands are used to control the nucleation and growth of the QDs [13], as well as their colloidal stability and surface passivation, so that they become less easily affected by the environment and solvents. Taking a closer look in figure 2.4 to the physical structure of a QD, two different parts can be noticed: an inner semiconductive core and an outer organic ligand coat, covering the quantum dot. The inner core can be build up

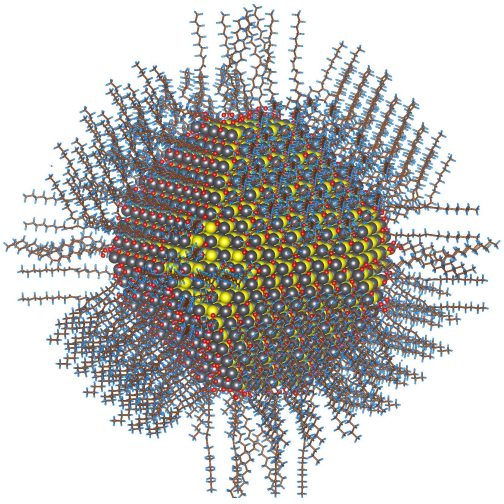

Figure 2.4: Colloidal nanoparticle; it can be distinguished the inner semiconductive core and the outer organic shell. Image from https://commons.wikimedia.org/w/index.php?curid=33602351.

choosing among various semiconductor nanoparticles, generally ranging from 1 to 10 nm (but this highly depends on the material).

The outer organic ligand shell consists of ligands that generally have a hydrophobic head (like amines, carbocyclic acids and phosphines) and a hydrophilic alkane or alkene tail usually from 8 to 18 carbon atoms long. Depending on the way ligands interact with the surface of the core, they can be

divided in three classes: L-type are charge neutral Lewis bases (electron donors) and bind to metal atoms at the surface, Z-type are neutral Lewis acids (electron acceptors) and bind to non metal atoms, and X-type are ionic species binding to the surface as ionic pairs.

At the end of section 2.1.2 we have seen that atoms at the emission quantum efficiency of a NC create surface trap states that quench the radiative recombination, thereby limiting the optical properties of a QD. The use of ligands mitigates this condition, contributing at the same time to the colloidal stability, which is the primary use of ligands for colloidal NCs. Furthermore, the length of the ligand used affects also the average distance between the QDs, when deposited on films, for instance, having effects on the radiative properties of a sample, as will be investigated in the following chapters.

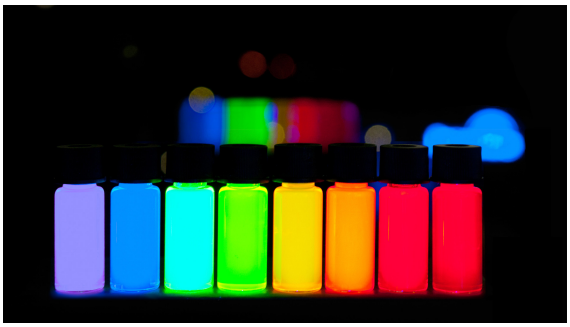

Figure 2.5: Colloidal QDs with gradually stepping emission from violet to deep red. Image from https://commons.wikimedia.org/w/index.php?curid=26950552.

2.3 Perovskites and lead halide perovskites

Perovskites are compounds described by the chemical formula ABX_3 (coming from the mineral calcium titanate $CaTiO_3$), where A and B are two cations, often very different in size (with A being larger than B), and X is an anion bound to both the cations [14] (deviations from the formula ABX_3 can also be obtained in case of partially or fully vacant A and B sites, or when they are replaced by a combination of more cations, forming double or quadruple perovskites). Crystallographic stability and probable structure of a perovskite can be described by two parameters: the tolerance Goldschmidt factor t, defined as the ratio of the distance A-X to the distance B-X in an idealized solid-sphere model, $t = (r_A + r_X)/\sqrt{2}(r_B + r_X)$, with r_A, r_B and r_X being the radii of the corresponding ions (in an ideal cubic perovskite crystal structure, the lattice constant a is given by $\sqrt{2}(r_A + r_X) = 2(r_B + r_X)$), and the ochtaedral factor μ, defined as the ratio $\mu = r_B/r_X$. If the value of t lies between 0.89-1.0, the perovskite's crystal structure is similar to the one of figure 2.6 **a** ($Pm\bar{3}m$ cubic space group, with B and X ions forming corner-sharing octahedra); lower t values instead arise less symmetric orthorhombic or rhombohedral structures, while larger hexagonal or tetragonal, but transitions between such structures are common heating the perovskite (generally being cubic at high temperatures).

A class of perovskites that over the last two decades has been identified among the most promising materials in photovoltaic and light-emitting devices are perovskites that have halides as their X anion (usually $X = Cl^-, Br^-, I^-$) [15]. In these Halide perovskites (HPs) the A cation can be either a monovalent alkali metal (commonly Cs^+) or an organic cation (like methylammonium (MA) or formamidinium (FA)), while B cation is usually divalent Pb^{2+} or Sn^{2+}. Halide perovskites generally have $0.81 < t < 1.11$ and $0.44 < \mu < 0.90$ [14], and therefore some of them crystallize in cubic-like strutures. This in not the case for fully inorganic, heavy metal HPs, where the size difference between the two cations A, B and the anion X causes a distortion in the crystal lattice. Example values for t and μ for some halide perovskites are reported in figure 2.6 **b**.

If the B cation of a halide perovskite happens to be lead, the perovskite assumes the formula

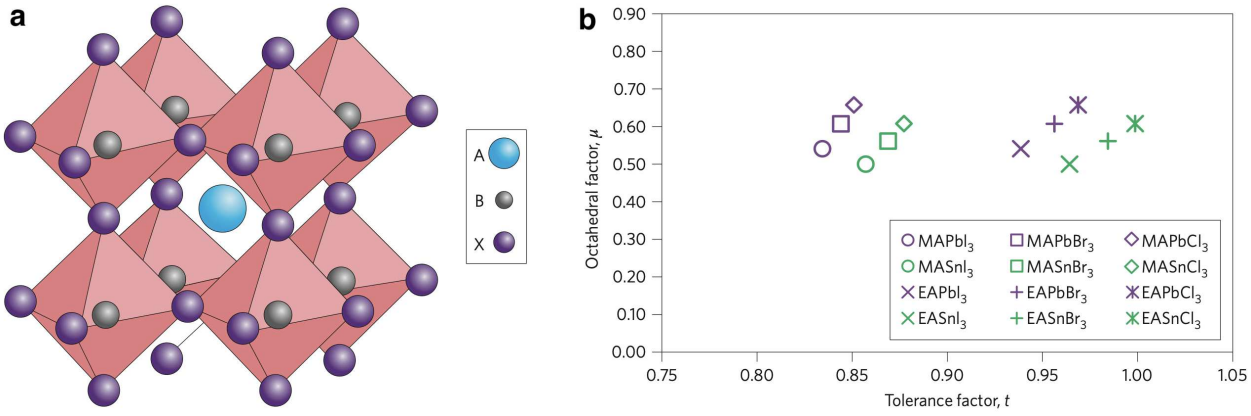

Figure 2.6: **a** Cubic perovskite crystal structure. The B cations are six-coordinated to the X anions forming corner-sharing BX_6 octahedra, and A cations are located in the framework cavities. **b** Values for t and μ for 12 different organic-inorganic halide perovskites of photovoltaic interests (hybrid organic-inorganic perovskites (HOIPs) are perovskites where A is an organic cation); the organic cations A are methylammonium (MA) and ethylammonium (EA), the anions X are halogens, B cations Pb and Sn are the most used for efficient cells. The pictures are taken from [14].

$APbX_3$, where A can be methylammonium (MA), formamidinum (FA) or cesium (Cs^+), and X is one or more halides. These so called lead halide perovskites (LHPs) have a direct bandgap. LHP NCs (mainly in the form with Cs) present some interesting properties compared to traditional semiconductor nanocrystals: they have a soft and ionic lattice and their optical and electronic properties are highly tolerant to structural defects and surface states.

IN particular, in this thesis $CsPbX_3$ NCs are studied (whose band structure is reported in figure 2.7, as well as the internal structure obtained via transmission electron microscopy). $CsPbX_3$ has an orthorhombic structure at room temperature, transforms then to a tetragonal phase at 373 K, followed by cubic phase at 403 K. Their ease of fabrication, strong solar absorption (due to bandgaps in the visible spectrum and NIR) and low non-radiative carrier recombination rates, make LHPs suitable for use in photovoltaic and light emitting devices [1]. One negative aspect of LHPs remains the toxicity of lead, raising issues during device fabrication, deployment and disposal.

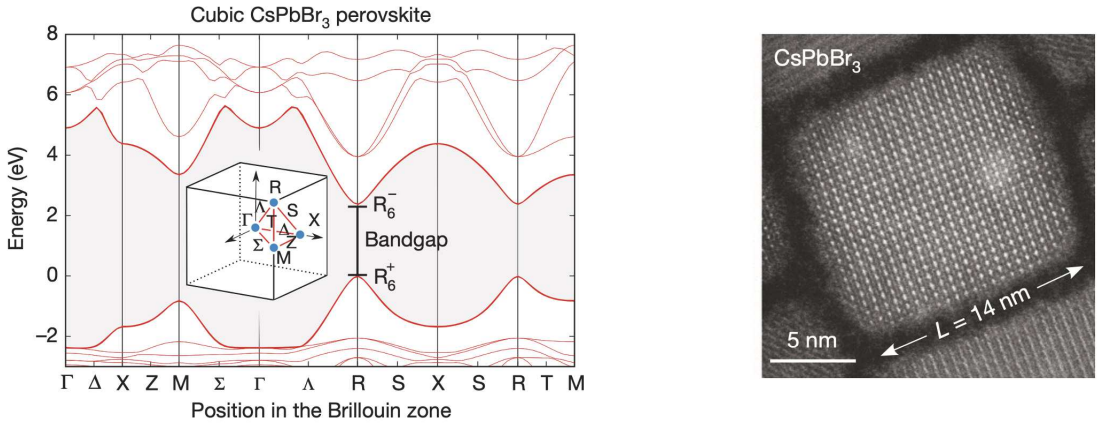

Figure 2.7: Left: band structure of $CsPbBr_3$ perovskite, where is shown the 1st BZ of the crystal; the bandgap lies at the R point. Right: transmission electron micrograph of an individual $CsPbBr_3$ nanocrystal with an edge length of 14 nm. Figures taken from [16].

2.4 Energy transfer processes between quantum dots

In section 2.1.3 we have seen that quantum dots smaller in size have an higher energy. In a sample containing for instance both small size and large size quantum dots, when these get excited by a laser part of the quantum dots will therefore initially be in an higher energy state than the others (in particular, smaller QDs have a smaller absorption cross section, so in the case of an equal ratio between large and small QDs, the larger QDs are more likely to be excited). If the different size QDs are close enough, it might happen through different mechanisms that a small QD, acting as a donor D, transfers energy to a large QD, acting as acceptor A (since the donor and acceptor are chemically identical, the energy transfer is homotransfer; if other molecules act as acceptors, it is called heterotransfer) [17].

In classical terms, this energy transfer can be seen as the interaction of two oscillating electronic dipoles. The donor dipole is initially oscillating, while the acceptor's dipole is at rest. The excitation is transferred from the from the first dipole to the second one because of the resonance condition.

In a quantum-mechanical description the system can be describe considering only the two electrons involved in the transition, one from the donor and one from the acceptor [17]. The anti-symmetrized wave functions for the initial state ψ_i (D excited, A unexcited) and final state ψ_f (D unexcited, A excited) are

$$\psi_i = \frac{1}{\sqrt{2}} \left(\psi_{D^*}(1)\psi_A(2) - \psi_{D^*}(2)\psi_A(1)\right) \tag{2.12}$$

$$\psi_f = \frac{1}{\sqrt{2}} \left(\psi_D(1)\psi_{A^*}(2) - \psi_D(2)\psi_{A^*}(1)\right) \tag{2.13}$$

Considering the interaction between donor and acceptor as a perturbation $\hat{V}$ of the hamiltonian of the sistem $\hat{H} = \hat{H_D} + \hat{H_A} + \hat{V}$, the interaction matrix element $\langle\psi_i|\hat{V}|\psi_f\rangle$ describing the coupling between the initial and final state is given by

$$U = \langle\psi_{D^*}(1)\psi_A(2)|\hat{V}|\psi_D(1)\psi_{A^*}(2)\rangle - \langle\psi_{D^*}(1)\psi_A(2)|\hat{V}|\psi_D(2)\psi_{A^*}(1)\rangle \tag{2.14}$$

The first term of equation 2.14 is called Coulombic term U_C; the second term is called the exchange term U_{ex} and represents the exchange of electrons, so the electrostatic interactions between charge clouds. Since the transfer occurs via overlapping of the electron clouds, it requires very close proximity between the donor and the acceptor. Assuming a dipole approximation (valid if the donor-acceptor distance is much larger than their dimensions), The transfer rate k_T is given by Fermi's golden rule

$$k_T = \frac{2\pi}{\hbar} |U|^2 \rho \tag{2.15}$$

with $|U|^2$ being a measure of the interaction between the initial and final state, ρ the density of states, and it is related to the overlap integral between the emission spectrum of the donor and the absorption spectrum of the acceptor.

If a photon is involved in the transfer process, being emitted by the donor and absorbed by the acceptor, a radiative transfer occurs. Radiative energy transfers are observed only when the average distance between the donor and the acceptor is larger than the wavelength of the emitted photon, and it depends on the spectral overlap and concentration (no interaction between D-A pairs is required). A non radiative transfer instead occurs at sub-wavelength distances and without the emission of a photon (as a result of an interaction between D-A pair, up to $\approx 20\,\text{nm}$). If the emission spectrum of the donor molecule overlap with the absorption spectrum of the acceptor molecule, donor and acceptor's vibronic transitions can couple and be in resonance. Such a non radiative energy transfer process is called resonance energy transfer (RET).

Depending on the strength of the coupling and the main interaction involved (either Coulombic and/or due to intermolecular orbital overlap), different RET processes can be defined. In case of very weak coupling consisting of long-range dipole-dipole interactions the RET is called Förster-type

resonance energy transfer (FRET, or fluorescence resonance energy transfer). Such process can be represented as (D*, A) $\overset{k_T}{\rightarrow}$ (D, A*), where * represent the excited states and k_T is the rate of resonance energy transfer between the donor and acceptor pair. In this process, the donor gets excited by an external photon and then transfers energy non radiatively to the acceptor leaving it in an excited state. The process is mediated by a so called "virtual photon". The Jablonski diagram of a FRET process is reported in figure 2.8. In our case, donors are represented by more energetic small (in size) QDs, while acceptors are less energetic large QDs. Indeed small molecules and 3D-confined QDs acceptors are considered to be infinitesimal transition dipoles. The rate of energy transfer k_T is given by [17]

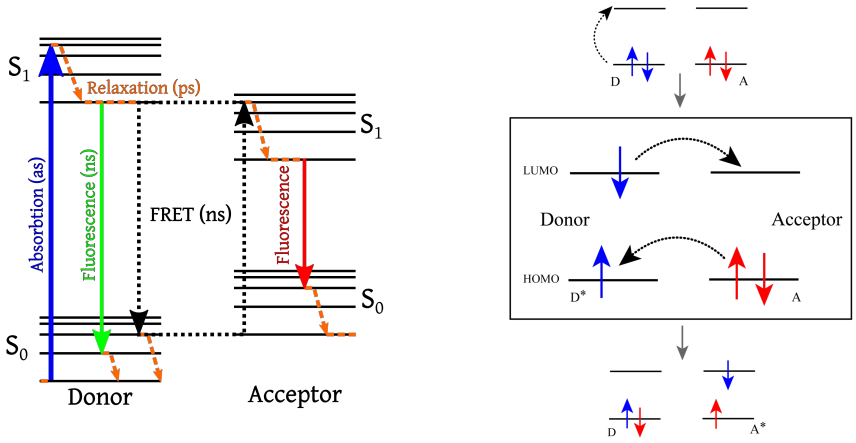

Figure 2.8: Left: Jablonski diagram of a FRET with typical timescales indicated; the black dashed line indicates a virtual photon. Right: schematics of a Dexter electron transfer. Pictures taken from https : //commons.wikimedia.org/wiki/File : FRET$_{\text{J}}$ablonski$_{\text{d}}$iagram.svg and https : //commons.wikimedia.org/wiki/File : Dexter$_{\text{e}}$lectron$_{(}$energy$)_{\text{t}}$ransfer.png.

$$k_T = \frac{1}{\tau_D}\left(\frac{R_0}{r}\right)^6 \tag{2.16}$$

where τ_D is the decay time of the donor in the absence of an acceptor, R_0 is the Förster radius, and r is the donor-to-acceptor distance. Due to the dependency r^{-6}, this process is strongly distance dependent. The FRET effciency, or the PLQY of the energy-transfer transition (so the fraction of photons absorbed by the donor whose excitation energy is transferred to the acceptor), is given by [18]

$$E = \frac{k_T}{k_r + k_T + \sum k_i} \tag{2.17}$$

where k_r is the radiative decay rate of the donor, k_T is the rate of the energy transfer and k_i the rates of any other non radiative de-excitation pathways.

An other type of RET is the Dexter-type energy transfer (or charge transfer). This process requires an overlap between A and D wavefunctions, and therefore occurs at short distances (tipically below 1 nm, unlike FRET that occurs with distances of about 10 nm [17]). A schematic of a Dexter transfer process is in figure 2.8. Unlike FRET, Dexter energy transfer can also occur between non-emissive electronic states of the materials (spin-allowed processes are based on the Wigner spin conservaiton rule).

Both FRET and Dexter are non radiative RET, with their main differences being their distance dependencies, the dependence of the overlap (spectral overlap for FRET between D emission and A absorption, electronic wavefunctions overlap for Dexter) and the mechanism involved (non-radiative dipole-dipole interaction between the D and A for FRET, direct exchange of electrons between D and A for Dexter).

Chapter 3

Experimental methods

3.1 Synthesis of $CsPbBr_3$ Quantum Dots

The size of the quantum dots can be varied during the synthesis, and can depend on many factors such as the ratio between the chemicals, the times between different steps of the synthesis, the temperature, which ligand is used etc. Since all these factors have a contribute, it is not always easy to synthesise quantum dots of the desired size. Often the ratio between the solvents should be varied in order to obtain smaller or larger QDs.

The chemicals used in the synthesis are the following: Lead bromide ($PbBr_2$, 99.999%), cesium carbonate (Cs_2CO_3, 99.9%), hexane ($\geq$ 99%), diisooctylphosphinic acid (DOPA, 90%), n-Octane (min. 99%), lecithin ($>$ 97% from soy), trioctylphosphine oxide (TOPO, min. 90%), heptane, chloroform ($CHCl_3$), didodecyldimethylammonium bromide (DDAB), acetonitrile (ACN).

Before the synthesis of the QDs, stock solutions of $PbBr_2$, Cs_2CO_3, TOPO and various lingands were synthesized. Accoridng to [13], the $PbBr_2$ stock solution (0.04 M) was prepared by dissolving $PbBr_2$ (1 mmol) and TOPO (4 mmol) in octane (5 mL) at 120°C, and then diluted in hexane (20 mL)(a minimum of a 4-fold excess of TOPO to $PbBr_2$ is necessary to fully solubilize $PbBr_2$ in hexane). The Cs-DOPA stock solution (0.02 M) was prepared by mixing Cs_2CO_3 (100 mg) with DOPA (1 mL) and octane (2 mL) at 120°C, followed by dilution with hexane (27 mL). The lecithin stock solution (0.13 M) was prepared by dissolving lecithin (0.5 g) in hexane (10 mL) at 70°C. The TOPO stock solution (0.2 M) was prepared by dissolving TOPO (4 mmol) in hexane (20 mL).

In order to achieve the desired sizes, the amount of solvents is varied. If the initial solvent is in larger quantity, during the synthesis the $PbBr_2$ and Cs_2CO_3 molecules are more distant and this results in QDs smaller in size. For the synthesis of the larger QDs, additional TOPO is used.

For the small size QDs ($d \approx 5 - 5.3$ nm), at room temperature 2.5 mL hexane and 300 μL of $PbBr_2$ stock solution were loaded in a vial. Under heavy stirring, 150 μL of Cs-DOPA stock solution was rapidly injected (in order to obtain high quality QDs, the injection of the Cs_2CO_3 stock solution has to be done very quickly). After 2 minutes, 0.5 mL of chloroform were added, after an other minute 150 μL of ligand (DDAB or lecithin) were added, and after another minute 1 mL of ACN was added. The solution was then centrifuged at 10000 rpm for 3 minutes, the solvent completely evaporated with pressure air and the QDs redispersed in 1 mL of octane. For the larg size QDs ($d \approx 10 - 11$ nm), always at room temperature 0.5 mL of hexane, 300 μL of $PbBr_2$ stock solution and 100 μL of TOPO stock solution were loaded in a vial, and 150 μL of Cs-DOPA stock solution was rapidly injected under heavy stirring. 2.5 mL of chloroform, 150 μL of ligand and 5 mL of ACN were added waiting the same times as previously, the QDs centrifuged and redispersed in 1 mL of octane. The absorption of the synthesized QDs was measured in situ with a spectrometer.

The QDs solution was then drop casted on a glass film (25 mm of diameter, previously cleaned in isopropanol using ultrasounds) and let it dry. The film was covered during the drying phase in order to have a more homogeneous distribution of the sample on the surface and to avoid back scattering.

3.2 Mixing different sizes

When mixing two types of QDs that are different in size, we want to achieve a known and predefined ratio between the number of large and small QDs, and therefore the concentration of the samples must be known. The intrinsic absorption coefficient μ_i is a useful parameter to do so [19] [20]; it is given by

$$\mu_i = \frac{A}{fL}\ln 10 \tag{3.1}$$

with A being the absorbance calculated from the in situ absorption spectra of the $CsPbBr_3$ QDs, L is the path length or thickness of the sample, and f the volume fraction. In a medium composed by dispersed QDs with a concentration c_{QDs}, according to Beer's law the absorbance is also given by $A = \varepsilon c_{QDs} L$, with ε being the molar absorption coefficient [19].

As it only depends on the optical parameters of the QDs and surrounding host, μ_i is a material property that characterizes the light absorption of QDs in a given solvent. The relation 3.1 shows that μ_i can be determined experimentally without knowing the size and shape of the QDs, only the volume fraction f has to be known. Once μ_i is known, f can therefore be calculated from 3.1.

Knowing f, the concentration of QDs of a specific size is give by

$$c_{QDs} = \frac{f}{V_{QD}\, N_A} \tag{3.2}$$

where N_A is the Avogadro's number, V_{QD} the spherical volume of the QDs (considering the dimension without the ligand, since it does not affect the absorbance). The actual concentration of the sample is given by $c_{sample} = c_{QDs}(V_{sample} + 2\,\mathrm{mL})/V_{sample}$.

Since in the mixed sample we want the number of small and large quantum dots to be know, and we want to keep it equal for both the ligands, the condition $\frac{c_{QDs}^{small}}{c_{QDs}^{large}} \approx const.$ has to be fulfilled, with the constant determined so that the PL and absorbance for both the ligands were noticeable in the mixed sample spectra. Now it is possible to prepare the mixed sample adding volumes of the two samples in the determined ratio.

3.3 Optical spectroscopy methods

The optical properties of the synthesized QDs are analyzed using different spectroscopy methods. The size and quality of the QDs were first determined by the steady-state absorption spectra, as well as their absorbance, PL and PLQY. Time resolved PL measurements were then performed in order to obtain a better characterization of the charge carrier dynamics.

3.3.1 Measurements of optical parameters with steady-state spectroscopy

When a sample is illuminated by light of a certain intensity I_0, part of the light is absorbed, leading to a reduced intensity I after the propagation through the sample (the light is also reflected and scattered, but this contributes are smaller and can be neglected in our case). When passing through a sample of thickness L, the intensity changes according to the Lambert-Beer law:

$$I(\lambda) = I_0(\lambda)\exp(-\alpha L) \tag{3.3}$$

with α being the absorption coefficient of the sample. The absorbance A (also called optical density OD) can than be obtained from the trasmittance $T = I/I_0$ of the sample as

$$A = -\log_{10} T = -\log_{10}\frac{I}{I_0} \tag{3.4}$$

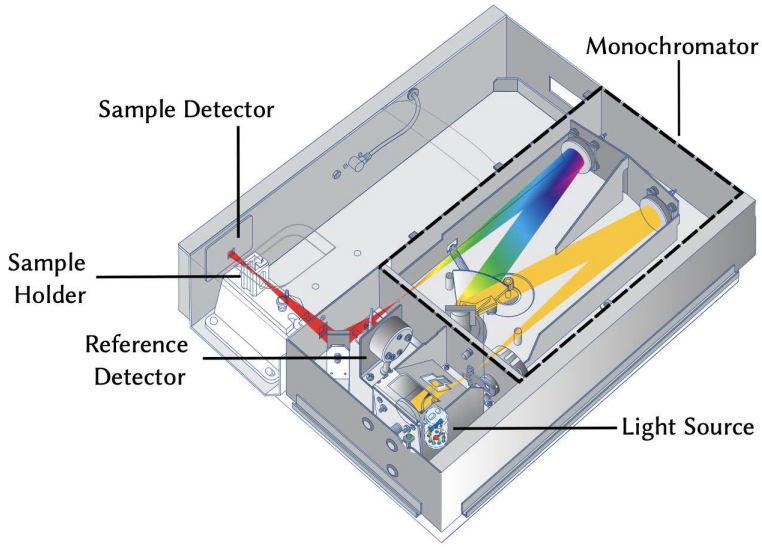

Figure 3.1: Schematics of a Cary 60 UV-Vis spectrometer. The light is spatially separated by a monochromator, and for every wavelength the intensities before and after the passage through the sample are measured. Figure taken from [21] [22].

Therefore knowing I_0 and I for every wavelength an absorbance profile can be obtained.

The absorbance spectra of the samples were acquired with a Cary 60 UV-Vis spectrometer by Agilent Technologies (schematic representation in figure 3.1). In this setup, white light coming from a xenon lamp is splitted in different wavelengths through a monochromator, which consists of a diffraction grating that spatially separates the individual wavelengths. The grating rotates and just one wavelength at a time passes through a slit. The outcoming monochromatic light is then partially splitted; one part is collected by a reference detector (this will be our I_0), while the other excites the sample in a cuvette, positioned in a sample holder. The transmitted intensity I is then measured by a silicon diode. Since the sample is diluted when measured, a correction due to the solvent has to be taken into account. This is done acquiring a baseline with the cuvette filled with the solvent only.

Besides the light "not passing" through the sample, also the light emitted by the sample after its excitation can be measured. A semiconductor QD in an excited state recombines after a certain time. The energy difference is emitted with a photon, and depending on the emitted photon wavelength a photoluminescence spectrum can be obtained. The steady-state PL measurements were performed on a Horiba Fluorolog-3 FL3-22 spectrometer. A desired wavelength coming from a xenon lamp is selected by a double grating monochromator and excites the sample. The PL emitted by the sample is collected at 90° from the excitation beam, passes through an other double grating monochromator and is detected by a photomultiplier tube. In this way a PL spectrum can be obtained.

If instead the excitation wavelength is changed and the intensity at a certain emission wavelength is detected, a photoluminescence emission (PLE) spectrum can be obtained. The radiative efficiency of the material can be characterized with the quantum yield. We have seen how the PLQY is the ratio between the number of photons emitted radiatively and the photons absorbed. Knowing the emission EM and excitation EX intensities for the sample and for a reference cuvette filled with the solvent, measured over an integrating sphere, the PLQY of the sample can be calculated referring to figure 3.2 as follows [4]:

$$\text{PLQY} = \frac{N_{em}}{N_{abs}} = \frac{EM_{\text{sample}} - EM_{\text{blank}}}{EX_{\text{blank}} - EX_{\text{sample}}} \tag{3.5}$$

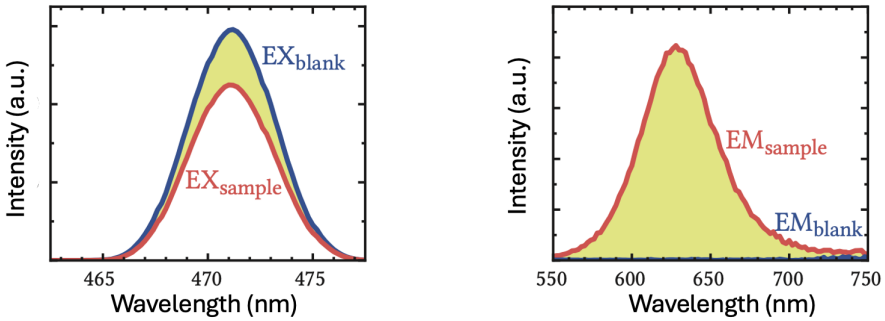

Figure 3.2: Left: excitation spectra for the sample and the reference; the highlighted area is proportional to the number of absorbed photons. Right: PL spectra for the sample and the reference; the highlighted area is proportional to the number of emitted photons. Pictures taken from [4].

3.3.2 Streak camera for time-resolved photoluminescence spectroscopy

In time-resolved spectroscopy the behaviour of the charge carriers is studied over time; for these measurement a *Hamamatsu Universal Streak Camera C10910* is used (a picutre of the setup is reported in figure 3.3). PL measurements with high time resolution are needed to resolve ultrafast processes

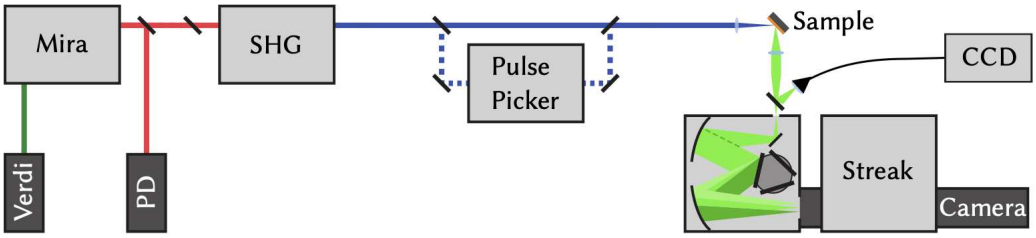

Figure 3.3: Streak camera setup. A CW *Verdi G12* pumps a Ti:sapphire in the cavity of the *Mira Optima 900-F* achieving population inversion. Through mode-locking laser pulses in the NIR region are generated. Part of the beam is reflected on a photodiode (PD) and triggers the streak camera, while the other is shifted to the UV-Vis using a SHG crystal. the repetition rate can be further varied with a pulse picker. The beam hits the sample and the PL is collected by a spectrometer, achieving wavelength resolution, and by the streak unit that provides time resolution. The resulting spectrum is recorded by a camera. Picture taken from [21].

like the exciton dynamic (for instance, the relaxation of charge carriers occurs in a time scale ranging from femto to picoseconds) [4], and in order to investigate such phenomena, the sample has to be excited with laser pulses shorter than the process considered. To achieve this a continuous wave (CW) *Verdi G12* laser (532 nm, 12 W) pumps a *Mira Optima 900-F* (schematics in figure 3.4), whose Ti:saphire (Ti:Al_2O_3) core emits light between 680 and 1100 nm. With a birefringent filter (BRF) a certain wavelength in this range can be selected ($\approx 800\,\text{nm}$ in our case). The Ti:saphire acts as a Kerr lens, and its refractive index varies depending on the light intensity as $n(I) = n_0 + n_2 I$, with n_0 and n_2 being the linear and non linear refractive index of the crystal. A vibrating glass (butterfly) leads to power fluctuations varying the path length of the cavity; once a mode has established, the vibration stops and just intense pulses are allowed to travel within the cavity. In this so called mode-locking condition, laser pulses at a repetition rate of $f_{rep} = 75.6\,\text{MHz}$ and pulse width of 200 fs in the near-infrared (NIR) region are generated.

When exiting the Mira, a small part of the laser beam is reflected onto a photodiode, and is used to trigger the streak camera. The NIR laser beam does not have a wavelength suitable for the excitation of most samples; for this reason it passes through a second harmonic generation (SHG) crystal, which shifts the wavelength in to the UV-Vis. The repetition rate can be varied with a pulse picker. The beam is then focused on the sample and their relative position can be adjust so that the first order

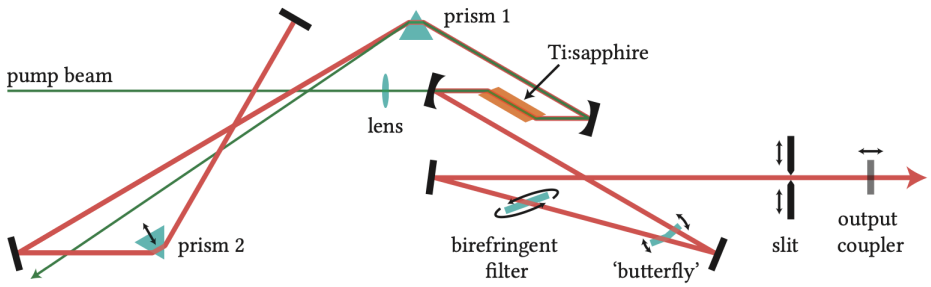

Figure 3.4: Schematics of the Mira Optima 900-F. The pump beam from the CW *Verdi G12* excites a Ti:saphire crystal. A certain wavelength is selected by a birefringent filter; a butterfly lens leads to power fluctuations, the Ti:saphire crystal works as a Kerr lens and focuses the high intensity modes that exit the Mira from a slit. [4].

reflection of the laser is blocked and the PL is focused on the entrance slit of the streak camera.

In the streak camera (schematically reported in figure 3.5), light passes through an horizontal slit and gets focused by lenses onto a photocatode. By photoelectric effect the photons are converted into electrons, whose wavelength is proportional to the energy of the generating photon and whose number is proportional to the intensity of the incoming light. The electrons are then accelerated in the streak tube. In the middle of the tube the electrons are vertically deflected by a capacitor with a time dependent voltage synchronized with the *Mira*. Initially the voltage is constant and all the

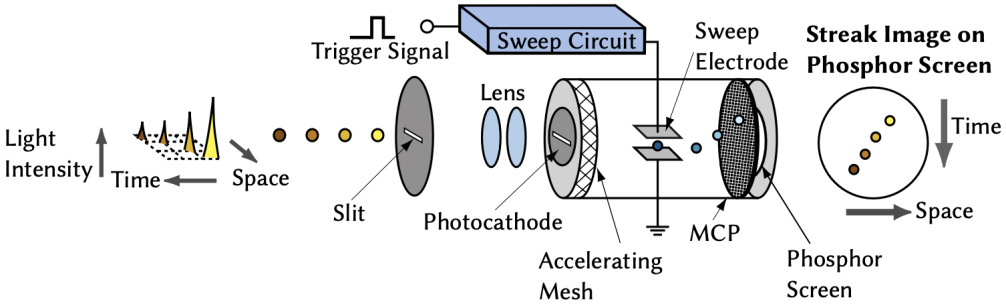

Figure 3.5: Schematics of the Hamamatsu Universal Streak Camera. Photons passing through the slit are focused on a photocatode. The electrons generated by photoelectric effect are accelerated and deflected by a capacitor proportionally to the time of arrival, multiplied by a MCP and reconverted into photons by a phosphor screen. Figure taken from [21] [23].

electrons reach the top of the phosphor screen; then a laser pulse triggers a sweep circuit and the voltage starts to decrease linearly until the electrons are deflected on the bottom of the screen, and this process is repeated every laser pulse. The voltage slope can be adjusted in a time range between 1 ns and 1 ms, according to the fact that if the sample is still emitting photons when the voltage is reset, arriving electrons will still be depicted on the screen. To prevent this so called back-sweep effect, the electrons are also horizontally deflected [4] with a second capacitor. The electrons pass then through a multi channel plate (MCP), getting multiplied up to a factor $\sim 10^4$, and finally are converted back in photons by a phosphor screen and detected by a CCD camera.

Chapter 4

Results

To study the energy transfers between $CsPbBr_3$ QDs, different sized $CsPbBr_3$ were synthesized based on the the synthesis method described in section 3.1. For this work, we tried to achieve the synthesis of monodisperse spheroidal quantum dots of two different sizes: larger ones with a diameter of $\approx 7\,\text{nm}$ and smaller ones with a diameter of $\approx 4\,\text{nm}$. During the synthesis, the QDs were coated with two different ligands (obtaining in this way a total of four samples different in size and ligand used). The ligands used are DDAB (shorter carbon chain length) and lecithin (longer). To roughly calculate the length of these two ligands one can consider the carbon carbon bond length and the carbon bond angle; in this way one can determine that the length each carbon adds to a ligand is $\approx 0.12\,\text{nm}$. Multiplying this value for the number of carbon atoms in the ligand carbon chain (12 for DDAB, 18 for lecithin), one gets the values of $\approx 1.5\,\text{nm}$ for DDAB and $\approx 2.3\,\text{nm}$ for lecithin. Being the two ligands different in length, one expects energy transfer processes to be more visible from the measurements of QDs capped with the shorter ligand, so DDAB, according to the energy transfer distance dependency described in section 2.4.

From the absorbance spectrum in solution, measured as described in 3.3.1, the QDs concentrations in solution can be calculated as described in 3.2. Assuming a value for the intrinsic absorption coefficient at 335 nm of $\mu_{i,335nm} = (1.59 \pm 0.05) \times 10^5\,\text{cm}^{-1}$ [24] (in the article $\mu_{i,335nm}$ is calculated for $CsPbBr_3$ QDs dispersed in n-hexane; in our case the solvent used is n-octane but we can assume the same value), the in situ absorbance A at 335 nm, and a path length L which in our case is 1 cm for the cuvettes used for measuring the absorbance, for different sizes and ligands the values in tab 4.1 are obtained. The concentration obtained refers to the QDs in the cuvette, which contains the sample diluted in 2 mL of octane.

ligand and size	Volume (nm^3)	A at 335 nm	f	c_{QDs} (mm^{-3})
DDAB small	36,1	0.082	$1.187 \cdot 10^{-6}$	$5.46 \cdot 10^{-14}$
DDAB large	164,6	0.102	$1.477 \cdot 10^{-6}$	$1.49 \cdot 10^{-14}$
lecithin small	41,6	0.288	$4.17 \cdot 10^{-6}$	$1.66 \cdot 10^{-13}$
lecithin large	179,6	0.351	$5.08 \cdot 10^{-6}$	$4.70 \cdot 10^{-14}$

Table 4.1: For QDs of different sizes and ligands these are the calculated parameter using the equations 3.1 and 3.2. The volume is obtained as $V = \frac{4}{3}\pi r^3$, where r is the radius of the QD.

Knowing the QDs concentrations, different sized QDs were mixed as described in 3.2, keeping a defined ratio between the number of large and small QDs of $\frac{c_{QDs}^{small}}{c_{QDs}^{large}} \approx 3.6$ (in particular, it was used ≈ 3.66 for the QDs coated with DDAB and ≈ 3.53 with lecithin).

Absorbance and PL of all the QDs in solution (so small, large and mixed coated with both ligands) were measured as described in section 3.3.1. The absorbance spectrum of semiconductor QDs presents several peaks, corresponding to the respective excitonic transitions allowed at certain excitation wave-

lengths, with the first excitonic peak lying energetically slightly above the energy band gap. Knowing from the absorbance spectrum the position of the first excitonic peak, the diameter size (in nm) of the QD can be derived as described in [13]. The resulting spectra measured for both ligands used are reported in figure 4.1 (first row for DDAB, second for lecithin). From the absorbance spectrum the first exciton peak can be identified at a wavelength of $\approx 468\,\text{nm}$ ($\approx 2.65\,\text{eV}$) for the small QDs coated with DDAB, and $\approx 497\,\text{nm}$ ($\approx 2.49\,\text{eV}$) for the large, while for the QDs coated with lecithin at $\approx 472\,\text{nm}$ ($\approx 2.63\,\text{eV}$) and $\approx 498\,\text{nm}$ ($\approx 2.49\,\text{eV}$) respectively. Knowing the first excitonic peak position, one can estimate the size of the QDs. According to [13], the nanocrystal diameters (without counting the ligand core shell thickness) are $\approx 4.1\,\text{nm}$ and $\approx 6.8\,\text{nm}$ for the samples **a** and **b**, and $\approx 4.3\,\text{nm}$ and $\approx 7\,\text{nm}$ for the samples **d** and **e**. Higher order excitonic peaks are also visible in the absorbance spectra at shorter wavelengths.

The PL emission peaks lie at $\approx 486\,\text{nm}$ ($\approx 2.55\,\text{eV}$) for small ones with DDAB and $\approx 508\,\text{nm}$ ($\approx 2.44\,\text{eV}$) for large, while for lecithin at $\approx 491\,\text{nm}$ ($\approx 2.53\,\text{eV}$) for the small and $\approx 507\,\text{nm}$ ($\approx 2.45\,\text{eV}$) for the large ones. As can be seen, the PL intensity peaks are red-shifted compared to the absorbance

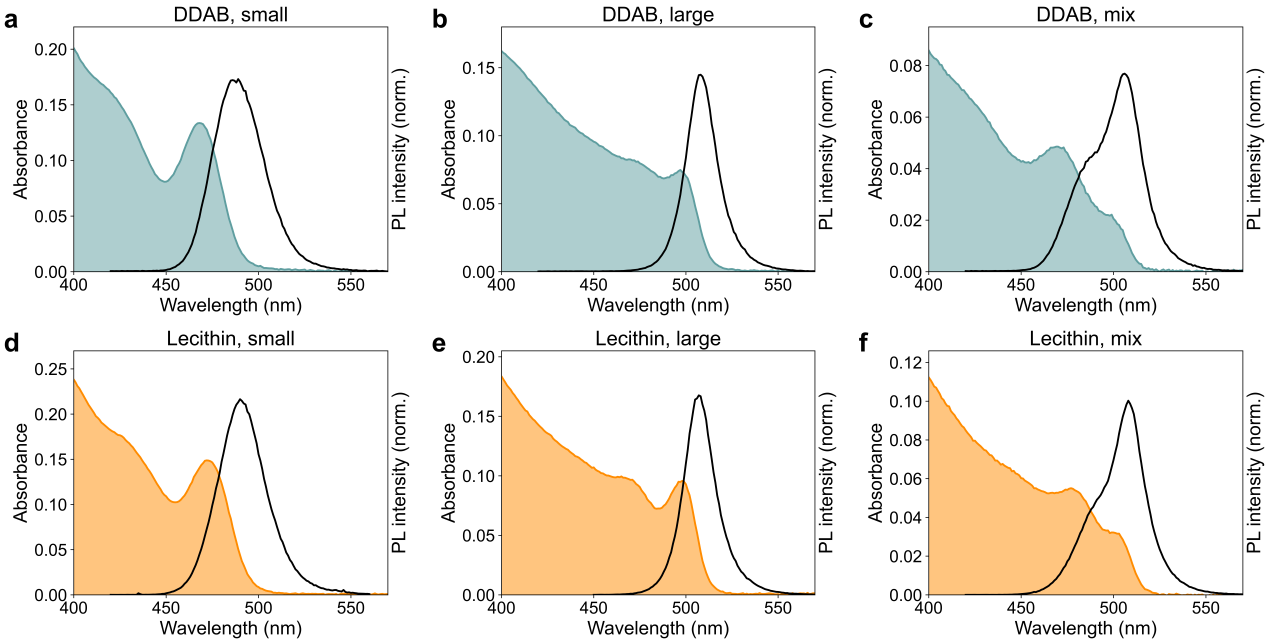

Figure 4.1: **a** Absorbance and PL intensity for small quantum dots with DDAB, **b** for large, DDAB, **c** mixed, DDAB, **d** small, lecithin, **e** large, lecithin and **f** mixed, lecithin. The PL intensity is normalized to a value that allows to distinguish the shape.

first excitonic peaks due to the Stokes shift [25], due to some energy lost as heat or through other non-radiative processes; the latter is less evident for large sized QDs ($\approx 9\,\text{nm}$ for both the ligands) than for small sized QDs ($\approx 18\,\text{nm}$).

Figures 4.1 **c** and **f** show the spectra of the mixed samples of small and large QDs, for DDAB and lecithin respectively, obtained as described in section 3.2 (so that the small and large QDs samples shown are the ones used to form the respective mixture). As can be seen from 4.1 **c** and **f**, for both ligands the PL and absorbance peaks of the mixed samples lie at the same wavelengths of their corresponding small and large components taken individually; for this reason, the PL and absorbance spectra of the mixed samples can be obtained as weighted sum of the relative PL and absorbance spectra taken as single contributes.

The PLQY values measure for both the ligands in solution and on film as described in section 3.3.1 are reported in table 4.2. It can be seen how, for every measured value, the PLQY on film is lower than in solution. This is due to many factors, such as the non radiative energy transfers, the appearance of surface defects during the deposition on film, reabsorption effects and other quenching

mechanisms induced by the substrate.

	DDAB (solution)	DDAB (film)	Lecithin (solution)	Lecithin (film)
Small QDs	59%	-	57%	32%
Large QDs	63%	-	75%	31%
Mixed QDs	57%	49%	56%	34%

Table 4.2: Experimental values obtained as described in section 3.3.1 of the PLQY for the measured samples in solution and on film. For small and large DDAB on film it was not meausred.

4.1 Photoluminescence in solution vs on film

When measuring the PL spectrum of the mixed QDs dispersed in solution, no or modest energy transfers between different size QDs are distant (in general, whit small or large QDs is intended the average size of the QDs inside the sample, but the size spectrum is broader for each sample due to intrinsic properties of the synthesis, and so energy transfers are expected also between QDs of the small and large samples only). In fact, in solution the different size QDs are distant enough that is very unlikely to have energy transfers (k_T is proportional to r^{-6} 2.16 in case of a FRET and decreases exponentially with the distance for Dexter-type, so for large distances it can be very small). With the QDs not able to interact through such processes over long distances (other processes, such reabsorption, are likely to happen also at greater distances), one should expect the PL spectrum of the mixed ones to be the sum of the single contributes of the large and small QDs inside the mixture. This is the case, as can be seen is figure 4.2 **a** and **c**, where for both the ligands used the weighted sum of the individual PL values of the small and large QDs (meaning the normalized sum of the experimental values for each energy) presents a shape comparable to the one obtained measuring directly the PL of the mixed QDs (in particular, PLs of the small and large QDs were multiplied by the two coefficients such that the resulting sum of the individual contributions has the minimum deviation from the experimental values). The PL intensity data for small and large QDs are rescaled so that the mix PL peak is normalized to one.

Decreasing the distance between the QDs, k_T increases, and so does the probability of energy transfers between different size QDs. If the distance is greatly reduced, with the QDs being very close, energy transfers are likely to happen. When a sample is deposited on a film, the distance between the quantum dots is strongly reduced. If the quantum dots are covered by a ligand shell the effective size of a quantum dot increases, and so the spacing between the nanoparticles when deposited on a substrate. Depending of the length of the ligand shell, the QDs deposited on a film will be more or less close to each other and therefore energy transfers more or less likely.

All the samples were deposited on a film and their PL and absorbance were measured in order to compare them with their counterparts measured in the solution. In figure 4.2 **b** and **d** for the two ligands the PL spectrum of the mixed QDs on film is obtained as sum of the individual small and large QDs PL experimental data, rescaled by the two factors that better approximate the experimental values of the mix. As expected, on the film the contribute in the PL given by the effective emission of small quantum dots only is smaller than the one in the solution (visually this contribute is represented by the area below the data set), because the ones that transmit energy emit as large QDs. Among the two ligands used, DDAB shorter than lecithin (has a shorter carbon chain length), therefore from similar emission ratios between small and large QDs we expect for DDAB a PL spectrum for the mixed QDs that resembles more the one of the large ones alone, because energy transfer processes are more likely to happen since the distance between QDs is smaller.

Knowing that the area under a PL curve is proportional to the number of emitting QDs (depending on the relative PLQY), one can calculate the ratios between the emitting small and large QDs in solution and on the film. The ratio between the areas A is equal to $\frac{A_l^{sol}}{A_s^{sol}} = \frac{N_l^{emitting}}{N_s^{emitting}} = \frac{N_l^{excited}\mathrm{PLQY}_l^{sol}}{N_s^{excited}\mathrm{PLQY}_s^{sol}}$,

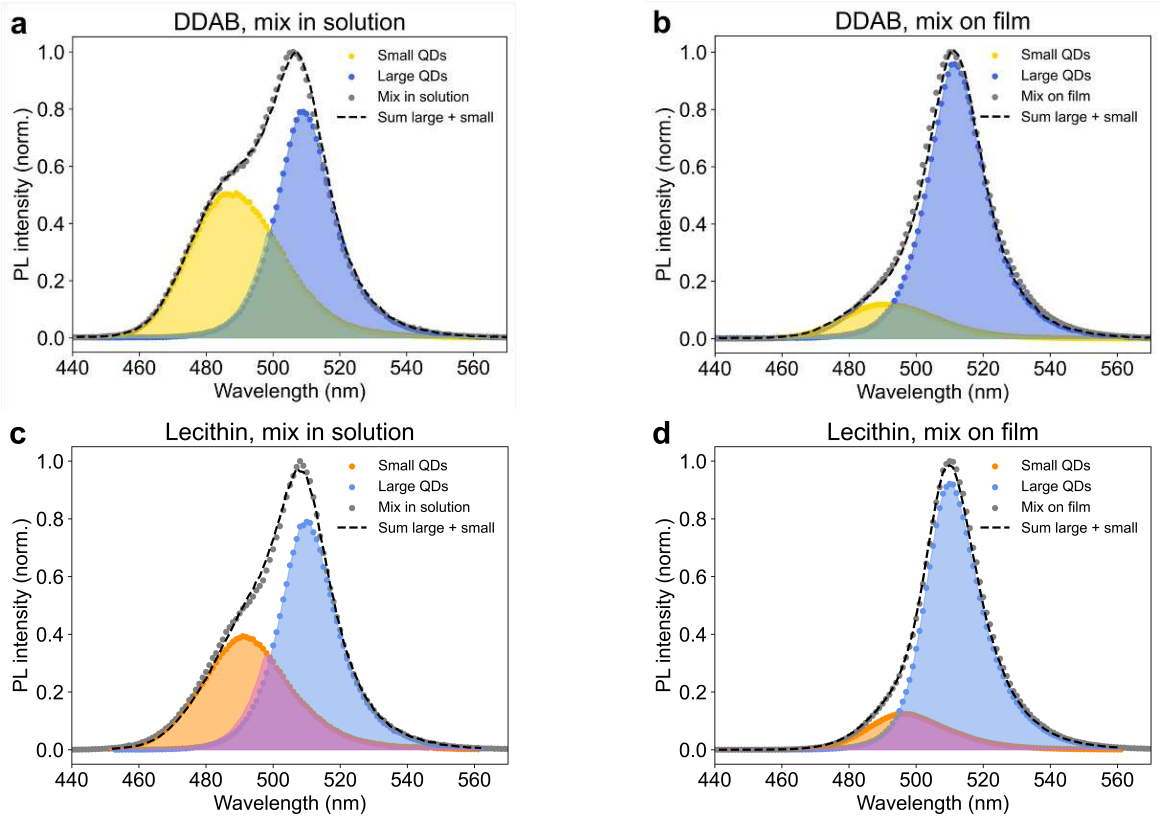

Figure 4.2: Comparison between the different ratios giving the PL in solution and on the film for both ligands. As can be seen, the area corresponding to the small QDs largely decreases for the figures **b** and **d**. This fact suggests the presence of energy transfers between smaller and larger QDs.

so the ratio between the excited QDs multiplied by their relative PLQY in solution, with s, l indicating the size. The ratios are ≈ 1.05 for DDAB and ≈ 1.42 for lecithin. Similar considerations for the ratios on the film allow us to calculate approximately the percentage of small QDs on the film that are involved in an energy transfer process. Starting from the assumption that energy transfers in the solution are negligible (which is a good assumption considering the distance dependence of the transfer processes), the ratio between the blue and red areas in figures 4.2 **b** and **d** is equal to $\frac{A_l^{film}}{A_s^{film}} = \frac{(N_l^{excited}+N_{s,T})\mathrm{PLQY}_l^{sol}}{(N_s^{excited}-N_{s,T})\mathrm{PLQY}_s^{sol}} = \frac{(N_l^{excited}+N_{s,T})\mathrm{PLQY}_l^{sol}}{N_s^{excited}\mathrm{PLQY}_s^{film}}$, with $N_{s,T}$ representing the number of small QDs involved in an energy transfer process. From the ratios in solution and the ratios on film one can calculate the ratio of small QDs that transfer on the total number of excited small QDs. Such ratio is $\frac{N_{s,T}}{N_s^{excited}} \approx 67\%$ for DDAB and $\approx 59\%$ for lecithin. The fact that the percentage of small QDs that transfer energy in DDAB is higher is something we expected, based on the considerations done previously about the length of the ligands.

In figure 4.2 we compared the difference in shape between the PL in solution and on the film, and concluded that this suggests the presence of energy transfers in the latter case. Is this enough to prove that the calculated amount of energy transfers actually happened? No. Several scenarios are also possible to explain the difference in the PL between the solution and the film. It can be that, when depositing the mixed sample on the film, areas on the surface of aggregation of large QDs create. This effect depends on how the QDs distribute on the film, and if the PL is measured on such areas, it will resemble the PL of large QDs. It can also be that the small QDs are partially quenched when deposited on the film, not contributing therefore to the total PL. Moreover, it can happen that a photon emitted by a small QDs gets reabsorbed exciting once again a large one.

PLE is a technique that can be used to study energy transfers. Looking at the PLE spectra of the

mixed QDs in solution and on film in figure 4.3 can help to rule out these other hypotheses: for the sample in figure 4.3 **a**, mixed QDs capped with DDAB on film, it can be seen that the normalized PLE spectrum, measured at an emission wavelength of 520 nm (i.e. at the PL maximum of the large QDs), overlaps reasonably well to the absorbance peaks of the mixed QDs (here in the graph is reported the absorption spectrum in solution for a better visualization, but the shape is almost the same of the one on film). This means that that the ratio of large and small QDs that absorb the excitation energy on film is the same as the ratio in the solution. For this reasons the presence of energy transfers between small and large QDs can be reasonably confirmed. For comparison, also the PLE of the mixed in solution is plotted (notice how it resembles the absorbance of the large QDs only); thus it can be concluded that FRET or Dexter-type energy transfer processes are the dominant energy transfer processes, rather than long range ones such reabsorption. A similar argument can be

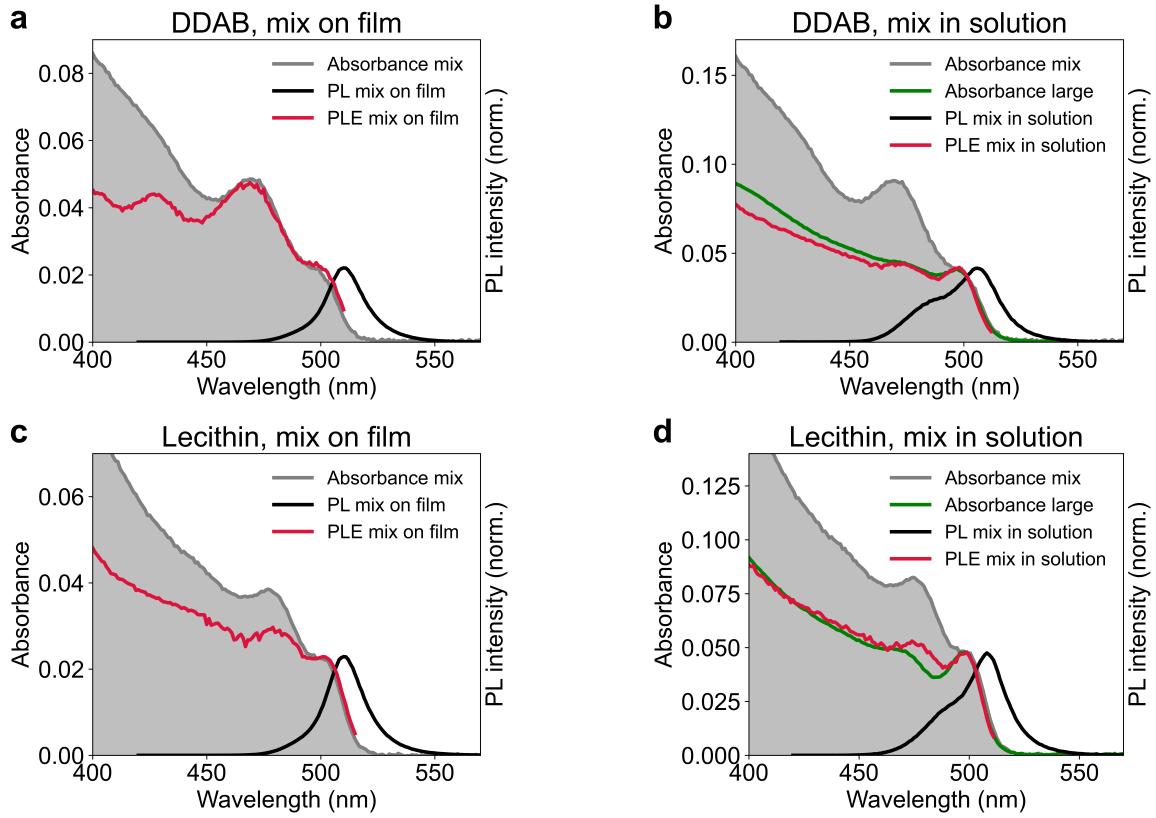

Figure 4.3: PLE with emission wavelength at 520 nm for **a** DDAB mix on film, **b** DDAB mix in solution, **c** lecithin mix on film and **d** lecithin mix in solution. Relative PL and absorbance spectra are also plotted as a comparison.

done for the mixed QDs capped with lecithin in figure 4.3 **c** and **d**. It can be clearly seen in **c** how the PLE's second peak (in correspondence of the absorption peak of the small QDs) does not resemble the absorbance spectrum as good as DDAB in figure **a**. This suggests once more how with lecithin energy transfers are less likely to happen compared with DDAB due to the longer length of the ligand. Again the PLE in solution presents a similar shape to the absorbance of the large QDs only.

The PLE spectra of figure 4.3 identifies short-range energy transfers to be the dominant energy transfer processes, over other far-field radiative processes such as reabsorption or other radiative transfers, long range interaction extending over hundreds of nm and depending on donor and acceptor concentrations in the sample, as well as their spectral overlap. Considering the spacing between the quantum dots, given on film mostly by the ligands, and considering the fact that the QDs are separated by a distance of two times the ligand length, FRET are most likely to be the type of energy transfer process involved, while Dexter type are very unlikely since they occur at distances even shorter

(tipically below 1 nm [17]).

4.2 Time-resolved measurements

Now we take a look at the time-resolved measurements taken with the Streak Camera as described in section 3.3.2. These have been done only with DDAB on film since, despite from the PLE spectra one can tell there is some energy transfer in lecithin capped QDs, the effect is expected to be more visible with DDAB coated QDs and on film.

The experimental values over time of the PL intensities at a given wavelength for the small and large QDs are reported in figure 4.4. The intensities are normalized and the wavelengths chosen are for both the sizes around their relative PL maxima. From the decay curves, one can find the lifetimes

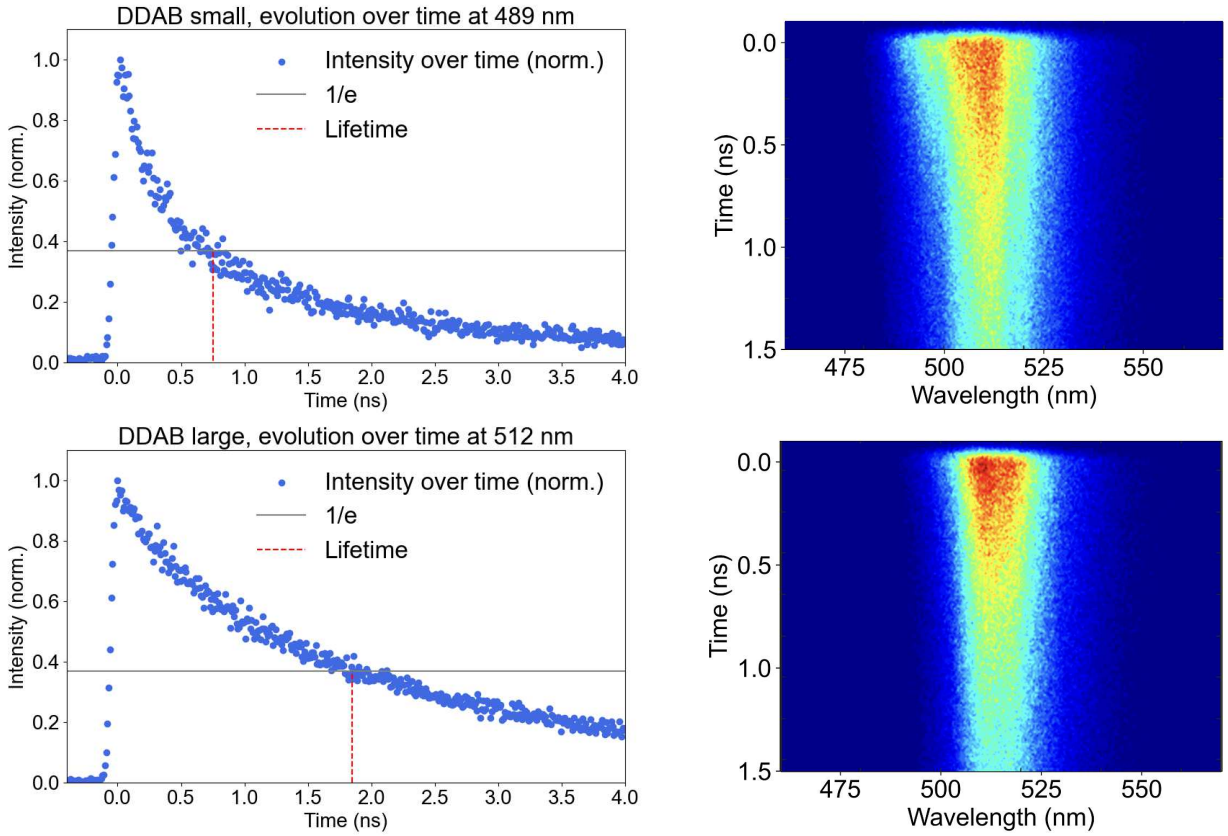

Figure 4.4: Left side: small and large QDs on film PLs over time at the wavelengths of 489 nm and 512 nm respectively. Right side: PL intensities over time at different wavelengths for small (above) and large (below) QDs on film for the first 1.5 ns; red color represents high intensities, blue color low ones.

for the small and large QDs in solution at their wavelength of maximum PL emission, so the time at which their intensity is reduced by a factor of e. For our samples the lifetimes are $\tau_s = 0.75\,\text{ns}$ for the small and $\tau_l = 1.85\,\text{ns}$ for the large QDs respectively. In figure 4.5 is plotted for the mixed film the time evolution at the same wavelengths used in 4.4, and the relative lifetimes in comparison with the ones obtained in 4.4. As it can be seen, the two exponential curves at 489 nm have approximately the same lifetimes, while for the two at 512 nm can be seen how the exponential for the mixed sample is less steep. Assuming the presence of energy transfers with small QDs acting as donors, one should expect the exponential curve for the mixed QDs at 489 nm to be more steep compared to the small QDs one at the same wavelength. This because in presence of energy transfers the small QDs present a further non radiative decay rate k_T, that brings on an average time small QDs to transfer and therefore emit as large QDs; the small QDs emitting as small QDs (so around 489 nm) are therefore

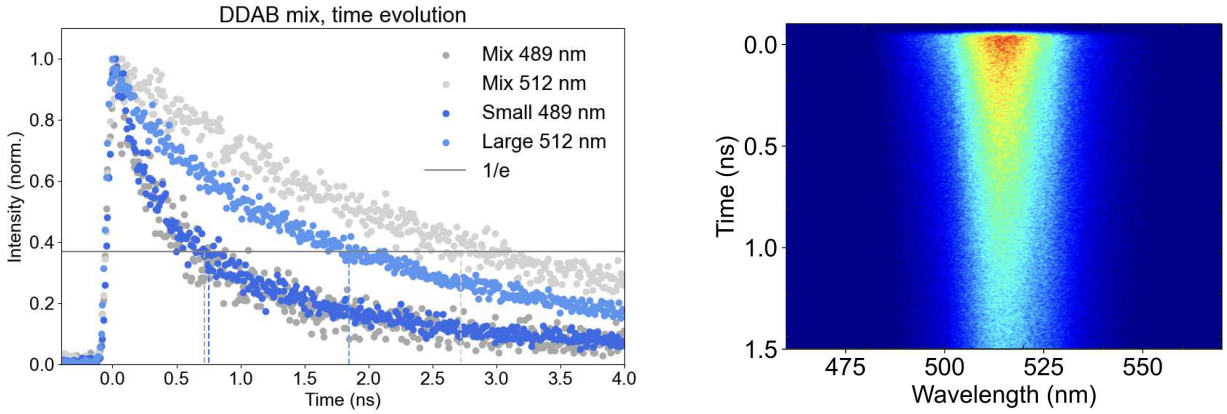

Figure 4.5: Left side: mixed QDs on film PLs over time at the wavelengths of 489 nm and 512 nm; comparison of the lifetimes with the data from figure 4.4. Right side: PL intensity over time of the mixed QDs on film at different wavelengths for the first 1.5 ns; red color represents high intensities, blue color low ones.

statistically on average quicker and their lifetime should be theoretically smaller than the one of small QDs only. This cannot be clearly seen from 4.5, and no conclusion about the effective presence of energy transfers can be done.

The reason why no such difference in the steepness is visible may be due to the fact that the transfer process happens at shorter time scales or other factors concerning the experimental conditions (for example it might has been excited a spot on the mixed film with only large QDs). The transfer decay constant k_T can be calculate as described in the following. The PLQYs for the small QDs in solution and on film are given by $\text{PLQY}_s^{sol} = \frac{k_r}{k_r+k_{nr}}$ and $PLQY_s^{film} = \frac{k_r}{k_r+k_{nr}+k_T}$. Knowing that $k_r + k_{nr} = \frac{1}{\tau_s}$,

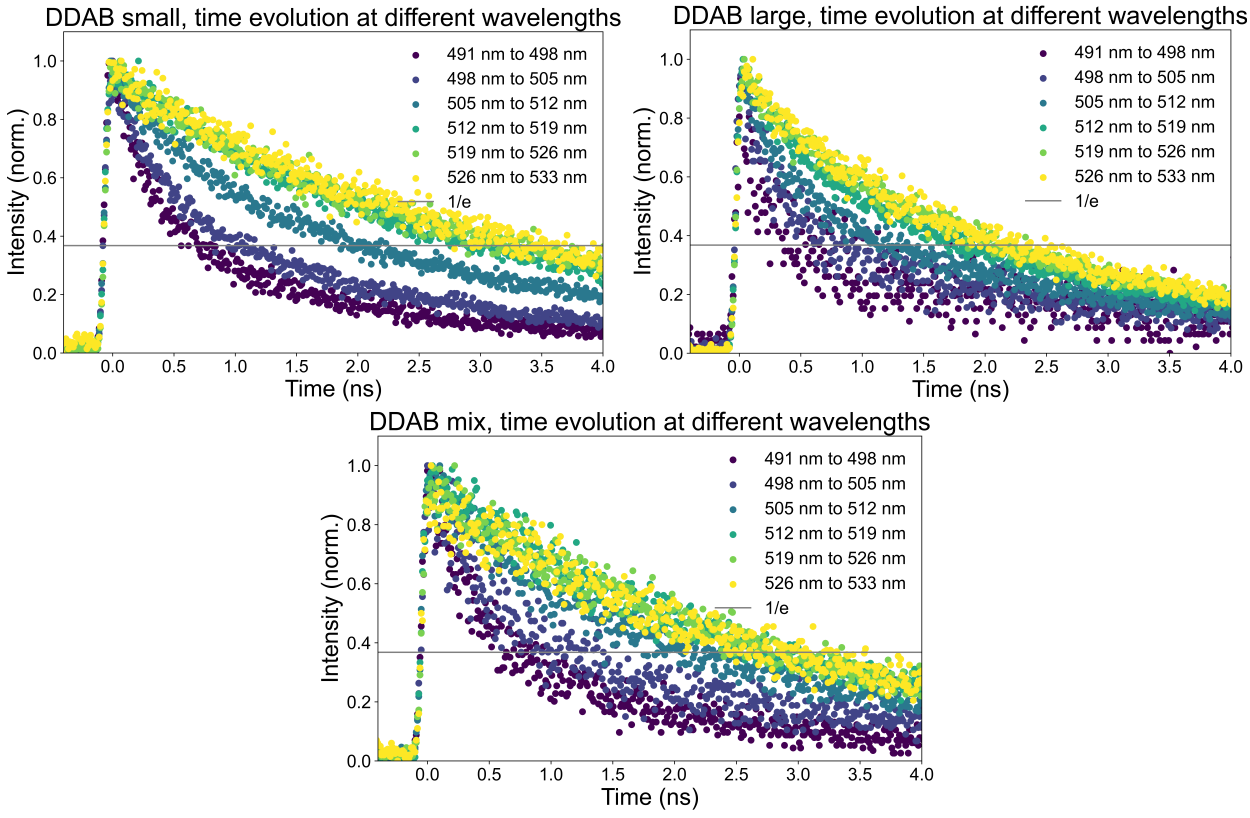

Figure 4.6: PL intensity over time for the three samples at six different wavelengths. It can be noticed how the lifetime increases increasing the wavelength and the difference in dispersion for small and large QDs.

where τ_s is calculated from the time evolutions of figure 4.4, and using the measured value for the PLQY in solution for the small QDs from table 4.2, one can find the values for the radiative and non radiative decay rates for the small quantum dots $k_r = 0.46\,\mathrm{ns}^{-1}$ and $k_{nr} = 0.87\,\mathrm{ns}^{-1}$. Knowing also the PLQY on film for the small ones (which was not measured in our case, it is indeed missing in table 4.2) one can calculate k_T.

In general a dispersion of the lifetimes for different wavelengths is noticeable not only for mixed, but also for small and large QDs. As can be seen in figure 4.6 in fact, every sample contains a distribution of different sized QDs inside it, between which energy transfers happen and whose statistical average gives the "size" of the sample. The synthesis of small QDs in particular gives a wide distribution of sizes inside the sample, which implies the PL decays not as a single exponential but as a stretched exponential. This is coherent with what can be seen in 4.6, where the distribution width of the lifetimes for the small QDs is larger than for the large QDs. To justify the larger steepness in the exponentials for lower wavelengths for all the three samples, we can use the same argument used before for 4.5, iterating it for all the wavelengths: supposing there is a rate k_T to transfer at a given wavelength, the QDs at this wavelength that do not transfer will be quicker on average and therefore have a shorter lifetime.

In figure 4.7 are plotted the cumulative sums over time normalized for small, large and mixed QDs. While the cumulative PL peaks for the large and the mix are in agreement with the corresponding ones measured with steady state spectroscopy, this is not the case for the small ones, that present a large shift to longer wavelengths. This is however anomalous because we are considering the integrated sum over an interval of $\approx 4\,\mathrm{ns}$, after which most of the QDs have emitted, and therefore the cumulative PL should look the same as the steady state PL, but this is not the case.

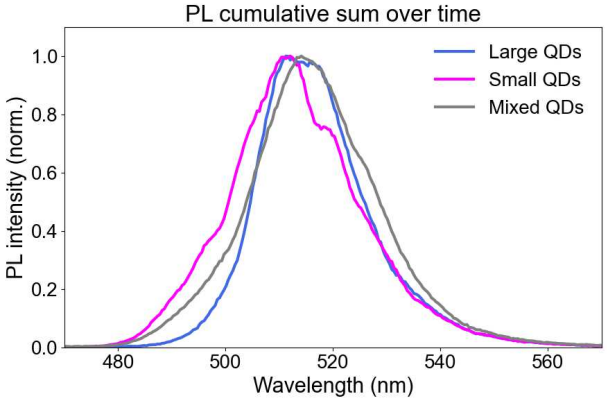

Figure 4.7: Sum of the PLs over time for time-resolved measurements of large, small and mixed samples on film.

Chapter 5

Conclusion

In summary, with this work it has been proven the presence of energy transfer processes between different size quantum dots, and its dependency on the distance between the nanoparticles, that can be adjusted varying the length of the ligand used.

With steady state measurements of PL and PLE, comparing the spectra obtained in solution and on film, it has been shown the presence of energy transfers between quantum dots of different sizes, when these are deposited on a film and their relative distance is greatly reduced. An estimation of the percentage of the small quantum dots involved in such energy transfer processes in also given. In particular, the length of the ligand played an important role in increasing the spacing between quantum dots, leading to a lower energy transfer percentage for quantum dots capped with lecithin respect to DDAB, which can be seen also from the PLE spectra, in agreement with the fact that lecithin is shorter than DDAB.

With time resolved measurements the emission wavelength dependency of the lifetimes for all the samples coated with DDAB has been shown, and it has been related once again with the energy transfers happening between smaller and larger quantum dots. However, it is not possible to infer such behavior comparing the lifetimes of the small and large quantum dots only with the mix at the same wavelengths.

Such results identify near field energy transfers as the dominant process of energy transfer, having a larger contribute to the change in the emission than other far-field energy transfers such as acceptor-donor reabsorption. Considering the spacing between the quantum dots due to the presence of the ligands, the dependence on the distance of the transfer decay rate and the spectral overlap, the major contribute to the energy transfers can be identified as FRET, without excluding a minor presence of also other types.

In general, this work helped to understand better how these processes work. Understanding these processes that govern the energy transfers between different size QDs provides insights into their collective behavior, how they can influence device efficiency and stability, and might result helpful to optimize device efficiency, design, and performance.

References

[1] Quinten A Akkerman, Gabriele Rainò, Maksym V Kovalenko, and Liberato Manna. "Genesis, challenges and opportunities for colloidal lead halide perovskite nanocrystals". In: *Nature materials* 17.5 (2018), pp. 394–405. DOI: https://doi.org/10.1038/s41563-018-0018-4.

[2] Mark Fox. *Optical Properties of Solids*. Oxford University Press, 2010.

[3] Steven H. Simon. *The Oxford Solid State Basics*. Oxford University Press, 2013.

[4] Alexander Florian Richter. "Charge Carrier Dynamics in Nontoxic Semiconductor Quantum Dots". PhD thesis. Ludwig-Maximilians-Universität München, 2020.

[5] Walter A. Harrison. *Electronic structure and the properties of solids : the physics of the chemical bond*. Freeman, 1980.

[6] Kwok K. Ng S.M. Sze. *Physics of Semiconductor Devices*. Wiley, 2006.

[7] Tadd Kippeny, Laura A. Swafford, and Sandra J. Rosenthal. "Semiconductor Nanocrystals: A Powerful Visual Aid for Introducing the Particle in a Box". In: *Journal of Chemical Education* 79.9 (2002), p. 1094. DOI: 10.1021/ed079p1094. eprint: https://doi.org/10.1021/ed079p1094. URL: https://doi.org/10.1021/ed079p1094.

[8] Markus Kantner. "Introduction". In: *Electrically Driven Quantum Dot Based Single-Photon Sources: Modeling and Simulation*. Cham: Springer International Publishing, 2020, pp. 1–14. ISBN: 978-3-030-39543-8. DOI: 10.1007/978-3-030-39543-8_1. URL: https://doi.org/10.1007/978-3-030-39543-8_1.

[9] Louis Brus. "Electronic wave functions in semiconductor clusters: experiment and theory". In: *The Journal of Physical Chemistry* 90.12 (1986), pp. 2555–2560. DOI: 10.1021/j100403a003. eprint: https://doi.org/10.1021/j100403a003. URL: https://doi.org/10.1021/j100403a003.

[10] Peter Reiss, Myriam Protière, and Liang Li. "Core/Shell Semiconductor Nanocrystals". In: *Small* 5.2 (2009), pp. 154–168. DOI: https://doi.org/10.1002/smll.200800841. eprint: https://onlinelibrary.wiley.com/doi/pdf/10.1002/smll.200800841. URL: https://onlinelibrary.wiley.com/doi/abs/10.1002/smll.200800841.

[11] Maureen A. Walling, Jennifer A. Novak, and Jason R. E. Shepard. "Quantum Dots for Live Cell and In Vivo Imaging". In: *International Journal of Molecular Sciences* 10.2 (2009), pp. 441–491. ISSN: 1422-0067. DOI: 10.3390/ijms10020441. URL: https://www.mdpi.com/1422-0067/10/2/441.

[12] Loredana Protesescu, Sergii Yakunin, Maryna I. Bodnarchuk, Franziska Krieg, Riccarda Caputo, Christopher H. Hendon, Ruo Xi Yang, Aron Walsh, and Maksym V. Kovalenko. "Nanocrystals of Cesium Lead Halide Perovskites (CsPbX3, X = Cl, Br, and I): Novel Optoelectronic Materials Showing Bright Emission with Wide Color Gamut". In: *Nano Letters* 15.6 (2015). PMID: 25633588, pp. 3692–3696. DOI: 10.1021/nl5048779. URL: https://doi.org/10.1021/nl5048779.

[13] Quinten A. Akkerman, Tan P. T. Nguyen, Simon C. Boehme, Federico Montanarella, Dmitry N. Dirin, Philipp Wechsler, Finn Beiglböck, Gabriele Rainò, Rolf Erni, Claudine Katan, Jacky Even, and Maksym V. Kovalenko. "Controlling the nucleation and growth kinetics of lead halide perovskite quantum dots". In: *Science* 377.6613 (2022), pp. 1406–1412. DOI: 10.1126/science.abq3616. eprint: https://www.science.org/doi/pdf/10.1126/science.abq3616. URL: https://www.science.org/doi/abs/10.1126/science.abq3616.

[14] Martin A Green, Anita Ho-Baillie, and Henry J Snaith. "The emergence of perovskite solar cells". In: *Nature photonics* 8.7 (2014), pp. 506–514. DOI: https://doi.org/10.1038/nphoton.2014.134.

[15] Quinten A Akkerman and Liberato Manna. "What defines a halide perovskite?" In: *ACS energy letters* 5.2 (2020), pp. 604–610. DOI: https://doi.org/10.1021/acsenergylett.0c00039.

[16] Michael A. Becker, Roman Vaxenburg, Georgian Nedelcu, Peter C. Sercel, Andrew Shabaev, Michael J. Mehl, John G. Michopoulos, S. G. Lambrakos, Noam Bernstein, John L. Lyons, Thilo Stöferle, Rainer F. Mahrt, Maksym V. Kovalenko, David J. Norris, Gabriele Rainò, and Alexander L. Efros. "Bright triplet excitons in caesium lead halide perovskites". In: *Nature* 553 (2017), pp. 189–193. URL: https://api.semanticscholar.org/CorpusID:1577411.

[17] Hilmi Volkan Demir Alexander Govorov Pedro Ludwig Hernández Martínez. "Understanding and Modeling Förster-type Resonance Energy Transfer (FRET)". In: *SpringerBriefs in Applied Sciences and Technology* (2016).

[18] Moens P. *Fluorescence Resonance Energy Transfer spectroscopy*. 2012. URL: https://web.archive.org/web/20160726180607/http://www.anatomy.usyd.edu.au/mru/fret/abot.html#frete.

[19] Zeger Hens and Iwan Moreels. "Light absorption by colloidal semiconductor quantum dots". In: *J. Mater. Chem.* 22 (21 2012), pp. 10406–10415. DOI: 10.1039/C2JM30760J. URL: http://dx.doi.org/10.1039/C2JM30760J.

[20] Quinten A. Akkerman. "Spheroidal Cesium Lead Chloride–Bromide Quantum Dots and a Fast Determination of Their Size and Halide Content". In: *Nano Letters* 22.20 (2022). PMID: 36215299, pp. 8168–8173. DOI: 10.1021/acs.nanolett.2c02601. eprint: https://doi.org/10.1021/acs.nanolett.2c02601. URL: https://doi.org/10.1021/acs.nanolett.2c02601.

[21] Lena Sophie Stickel. "Excitation Transfer from Perovskite Quantum Dots to Anchored Molecules". MA thesis. Georg-August-Universität Göttingen, 2023.

[22] Agilent Technologies. *Measuring baseline-corrected spectra on a Cary 60 UV-Vis*. 2011.

[23] Hamamatsu. *Guide to Streak Cameras*. 2008.

[24] Jorick Maes, Lieve Balcaen, Emile Drijvers, Qiang Zhao, Jonathan De Roo, André Vantomme, Frank Vanhaecke, Pieter Geiregat, and Zeger Hens. "Light Absorption Coefficient of CsPbBr3 Perovskite Nanocrystals". In: *The Journal of Physical Chemistry Letters* 9.11 (2018). PMID: 29790351, pp. 3093–3097. DOI: 10.1021/acs.jpclett.8b01065. eprint: https://doi.org/10.1021/acs.jpclett.8b01065. URL: https://doi.org/10.1021/acs.jpclett.8b01065.

[25] *"Fluorescence Microscopy - Basic Concepts in Fluorescence — Olympus LS"*. 2024. URL: https://www.olympus-lifescience.com/en/microscope-resource/primer/techniques/fluorescence/fluorescenceintro/.